



Communications
Research Centre
Canada
An Agency of
Industry Canada

Centre de recherches
sur les communications
Canada
Un organisme
d'Industrie Canada

Design of Dual-Polarized Probe-Fed Microstrip Patch Antennas for MIMO Application

Nicolas Gagnon, Aldo Petosa and John Bradley

CRC Report No. CRC-RP-2007-02
Ottawa, June 2007

IC

CAUTION

*This information is provided with the express understanding
that proprietary and patent rights will be protected*

LKC
TK
5102.5
.C673e
#2007-
002

ada

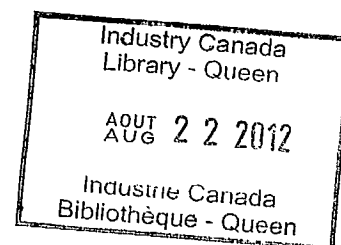
CRC

Design of Dual-Polarized Probe-Fed Microstrip Patch Antennas for MIMO Application

Nicolas Gagnon, Aldo Petosa and John Bradley

CRC Report No. CRC-RP-2007-02

Ottawa, June 2007



CAUTION

This information is provided with
the express understanding that
proprietary and patent rights will
be protected

<This page intentionally left blank>

Abstract

This document presents a probe-fed, dual-port, dual-polarized microstrip patch antenna to be used in a multiple-input multiple-output (MIMO) configuration for a mobile military communications system. The design and fabrication of the antenna are explained in detail. Scattering parameters (S-parameters) and far-field radiation patterns are provided for simulation and measurement cases. The antenna achieves a return loss of 15 dB, an isolation between ports of 35 dB and a maximum gain of 8.5 dBi within the frequency band of interest. In addition, an experimental study of coupling between two adjacent antennas was conducted. This study confirms that the worst case coupling is -15 dB, which should be acceptable for this kind of application. Furthermore, simulations were conducted to model the effect on the far-field radiation patterns of the antenna when mounted on the designated military vehicle. The major effects on the radiation patterns were the appearance of ripples, a higher cross-polarization level, sidelobes near the end-fire direction and a slight beam deformation; however, none of these effects were significant enough to seriously affect the operation of the antenna.

Résumé

Ce document présente une antenne à deux ports et à polarisation double de type plaque microruban alimentée par sondes. Cette antenne servira dans un système de communication militaire utilisant la technologie MIMO (entrées multiples, sorties multiples). La conception et la fabrication de l'antenne sont expliquées en détails. Les paramètres de dispersion (paramètres S) et les diagrammes de rayonnement en champ éloigné sont fournis pour les cas de simulations et de mesures. Les caractéristiques de cette antenne, dans la bande de fréquences d'intérêt, sont : un affaiblissement de réflexion de 15 dB, une isolation entre les ports de 35 dB et un gain maximal de 8,5 dBi. De plus, une étude expérimentale de couplage entre deux antennes adjacentes fut menée. Cette étude a confirmé que le pire cas de couplage est de l'ordre de -15 dB, ce qui devrait s'avérer acceptable pour une telle utilisation. D'autre part, des simulations ont été menées pour modéliser l'effet sur les diagrammes de rayonnement en champ éloigné lorsque l'antenne est installée sur le véhicule militaire désigné. Les effets les plus significatifs sur les diagrammes de rayonnement furent l'apparition d'ondulations, l'augmentation du niveau de polarisation croisée, l'apparition de lobes latéraux près du rayonnement longitudinal et une légère déformation du faisceau électromagnétique principal; cependant, aucun de ces effets n'est assez sérieux pour compromettre le bon fonctionnement de l'antenne.

Acknowledgements

The authors would like to thank David Lee for his helpful technical assistance, particularly in setting up the antenna for radiation pattern measurements.

The photographs presented in Chapters 1, 2 and 4 were taken by John Brebner.

Table of Contents

Abstract	i
Résumé	i
Acknowledgements	ii
Table of Contents	iii
List of Figures	iv
List of Tables	vi
1. Introduction.....	1
2. Antenna Design.....	3
2.1. Specifications	3
2.2. Antenna Design and Parts.....	4
2.2.1. Patch antenna and patch substrate	4
2.2.2. Lexan frame and air substrate	4
2.2.3. Thick ground plane	6
2.2.4. Connectors and probes	8
2.3. Antenna Assembly.....	10
2.3.1. Connector installation	10
2.3.2. Frame installation	10
2.3.3. Antenna substrate installation.....	10
2.3.4. Probe soldering	10
3. Results	15
3.1 Scattering Parameters.....	15
3.2 Radiation Patterns	15
3.3 Conclusions	20
4. Coupling Study	23
5. Simulations on Vehicle	27
5.1 MIMO antenna simplified model	27
5.2 MIMO antenna on vehicle simulations.....	29
5.2.1 Effect of meshing resolution on radiation patterns.....	35
5.2.2 Effect of physical ground on radiation patterns.....	38
6 Conclusions.....	39
References	41
Appendix A: Technical Drawings	43
Appendix B: S-Parameter Measurement Results	47
Appendix C: Far-field Measurement Results	53

List of Figures

Figure 1: Representation of antennas used in a MIMO system.....	1
Figure 2: Schematic representation of the MIMO antenna (approximately to scale) a. top view (showing frame underneath patch substrate); b. bottom view.	5
Figure 3: The patch antenna etched on its substrate a. front view; b. back view (units on ruler are centimetres).....	7
Figure 4: Lexan frame and SMA connectors (units on ruler are centimetres).....	8
Figure 5: The thick ground plane aluminium plate a. top view; b. bottom view (units on ruler are centimetres).....	9
Figure 6: Installation of the connectors to the thick ground plane aluminium plate (screws not shown) a. top view; b. bottom view (units on ruler are centimetres).....	11
Figure 7: Installation of the Lexan frame (units on ruler are centimetres).....	12
Figure 8: Fully-assembled antenna a. front view; b. back view (units on ruler are centimetres).....	13
Figure 9: Scattering parameters of the MIMO antenna (RAATLab unit) a. simulated; b. measured.	16
Figure 10: Front view of the mount used in the far-field anechoic chamber a. without antenna; b. with antenna.....	17
Figure 11: Side view of the mount used in the far-field anechoic chamber a. without antenna; b. with antenna.....	18
Figure 12: Tower of the far-field anechoic chamber with MIMO antenna (RAATLab unit) a. full view; b. close view.....	19
Figure 13: MIMO antenna mounted on the tower of the far-field chamber showing absorbing material covering the metal plate and posts.	20
Figure 14: Far-field radiation patterns of the MIMO antenna (RAATLab unit) for vertical polarization (port 1) at lower frequency (2.025 GHz) a. simulated; b. measured.	21
Figure 15: Measured gain versus frequency for the MIMO antenna (RAATLab unit).	22
Figure 16: Two MIMO antennas on the special jig designed to measure the coupling.....	23
Figure 17: Schematic view of the coupling experiment including port and separation definitions.....	24
Figure 18: Coupling between ports as a function of distance (worst case coupling within operating band shown).....	25
Figure 19: A LAV III from the Canadian forces (Photo: Department of National Defence).....	27
Figure 20: The LAV III model used for simulation.....	28
Figure 21: Scattering parameters of the simplified MIMO antenna model.....	29
Figure 22: Simulated far-field radiation patterns of the simplified MIMO antenna for vertical polarization (port 1) at lower frequency (2.025 GHz).	30

Figure 23: Empire™ 3D view of the LAV III model with MIMO antenna on top of the tower.....	31
Figure 24: Empire™ 3D view of the LAV III model showing 3D far-field radiation pattern of the MIMO antenna on top of the tower.	31
Figure 25: Simulated far-field radiation patterns of the simplified MIMO antenna for vertical polarization (port 1) at lower frequency (2.025 GHz) on top of the LAV III tower.	32
Figure 26: Empire™ 3D view of the LAV III model with MIMO antenna on the back of the shell.....	32
Figure 27: Empire™ 3D view of the LAV III model showing 3D far-field radiation pattern of the MIMO antenna on the back of the shell.	33
Figure 28: Simulated far-field radiation patterns of the simplified MIMO antenna for vertical polarization (port 1) at lower frequency (2.025 GHz) on the back of the LAV III.....	33
Figure 29: Empire™ 3D view of the LAV III model with MIMO antenna on the side of the shell.....	34
Figure 30: Empire™ 3D view of the LAV III model showing 3D far-field radiation pattern of the MIMO antenna on the side of the shell.	34
Figure 31: Simulated far-field radiation patterns of the simplified MIMO antenna for vertical polarization (port 1) at lower frequency (2.025 GHz) on the side of the LAV III.....	35
Figure 32: Simulated far-field radiation patterns of the simplified MIMO antenna for vertical polarization (port 1) at lower frequency (2.025 GHz) on top of the LAV III tower corresponding to Case 2 in Table V.....	37
Figure 33: Simulated far-field radiation patterns of the simplified MIMO antenna for vertical polarization (port 1) at lower frequency (2.025 GHz) on top of the LAV III tower corresponding to Case 3 in Table V.....	37
Figure 34: Simulated far-field radiation patterns of the simplified MIMO antenna for vertical polarization (port 1) at lower frequency (2.025 GHz) on the side of the LAV III with perfect electric conductive layer underneath.	38
Figure 35: Patch and substrate technical drawing (approximate patch dimensions).	43
Figure 36: Lexan frame technical drawing.....	44
Figure 37: Thick ground plane aluminium plate technical drawing.	45
Figure 38: Connector technical drawing.	46
Figure 39: S-parameters measured results for MIMO antennas.....	47
Figure 40: Measured far-field patterns for MIMO antenna (RAATLab unit).	53

List of Tables

Table I: Color legend for Figure 2.....	6
Table II: Performances of the MIMO antenna.....	22
Table III: Discretization data for the two MIMO antenna simulation cases.	29
Table IV: Figure description for MIMO antenna mounted on a LAV III.	30
Table V: Discretization data for the three simulation cases of MIMO antenna on top of the tower.....	36

1. Introduction

Multiple-input multiple-output (MIMO) refers to the application of multiple antennas, transmitters and receivers in terrestrial wireless communication systems. The MIMO architecture takes advantage of the multiple reflections of signals present in a multi-path environment and can lead to an impressive increase in performance [1]. Figure 1 shows an example of a representation of antennas used in a MIMO system.

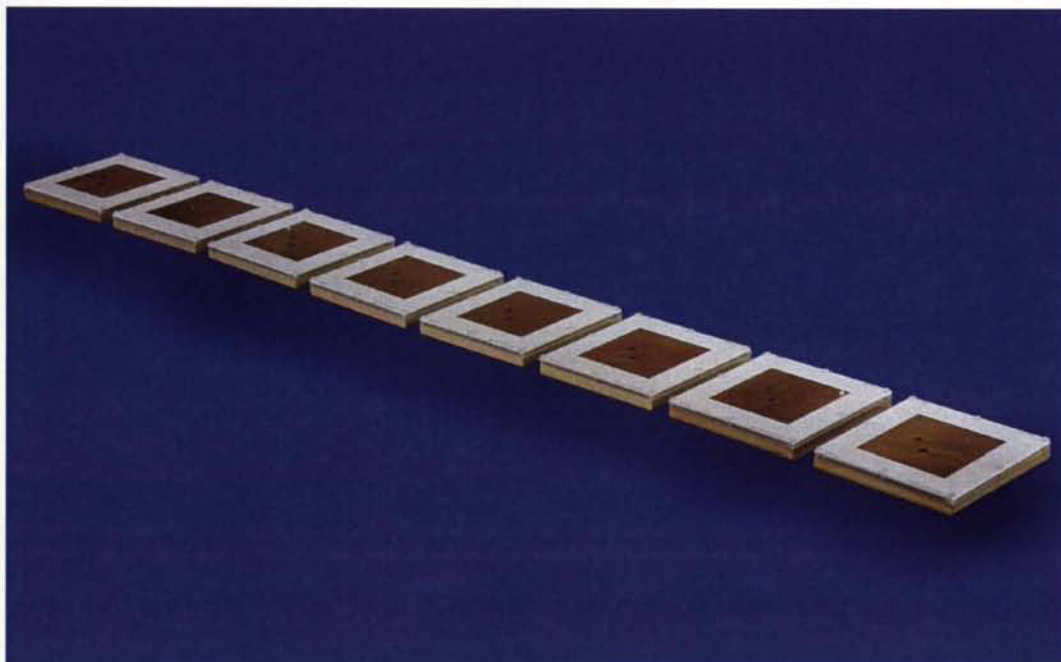


Figure 1: Representation of antennas used in a MIMO system.

As part of a collaboration with the Radio Communications Technologies (RRCT) group, the Advanced Antenna Technology (RAAT) group developed an antenna to be used for a MIMO application in the Military Mobile Radio Project. This report describes the antenna designed for this application.

The report is organized as follows:

- Chapter 2 presents the design of the MIMO antenna, including specifications, antenna components and assembly;

- Chapter 3 presents the results, including simulation and measurement results for scattering parameters (S-parameters) and far-field radiation patterns;
- Chapters 4 and 5 present additional work performed on the MIMO antenna, respectively a coupling analysis experimental study and antenna far-field simulations on vehicle;
- Chapter 6 presents conclusions.

2. Antenna Design

2.1. Specifications

The following specifications were required for the MIMO antenna:

- frequency band of 2.025–2.050 GHz;
- low-profile / planar architecture;
- use of orthogonal polarisation;
- wide radiation beam;
- input impedance of 50 Ω ;
- mechanical robustness.

In order to achieve the specifications, the following decisions were taken:

- the antenna type was chosen to be a microstrip patch antenna for its planar architecture, mechanical robustness, low-cost and simplicity;
- the microstrip patch antenna was also chosen for its capability to achieve a wide radiation beam and the use of a single antenna element for orthogonal polarisation;
- in order to achieve the bandwidth requirements, an electrically-thick antenna substrate was necessary;
- the dielectric constant of the antenna substrate was chosen between 3 and 4 to ensure for both a large enough electrical thickness and efficient radiation;
- an air layer was used between the ground plane and the patch substrate to further increase the electrical thickness and, consequently, the bandwidth;
- for mechanical purposes, the air layer was realized using a plastic frame to support the patch substrate;
- the microstrip patch antenna was fed using probes;
- for simplicity, no microstrip feed layer was used, instead the patch antenna was directly fed by SMA connectors (the inner conductor of the

SMA connectors was extended up to the patch antenna layer and used as probes to feed the patch);

- for good match and good isolation, the connectors were placed near the centre of the patch (i.e. at the $50\ \Omega$ points);
- a thick ground plane was used for mechanical purpose, i.e. robustness and support for the connectors.

2.2. Antenna Design and Parts

The design layout for the antenna is shown in Figure 2. The colors used refer to different parts of the antenna and are described in Table I. The following subsections describe the design of the individual parts of the antenna.

2.2.1. Patch antenna and patch substrate

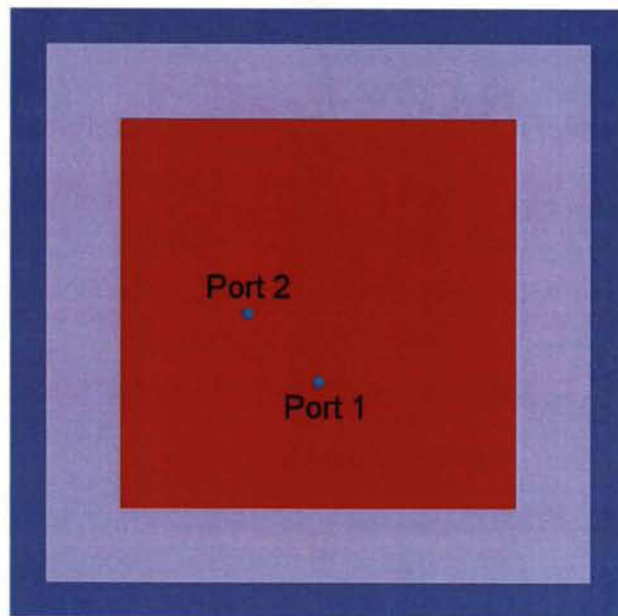
The patch antenna was designed to resonate at midband, i.e. at 2.0375 GHz. This allowed for an optimal resonance bandwidth. The size of the patch was very critical in order to allow the antenna to resonate exactly at this frequency. In fact, the antenna was tuned to a precision of $50\ \mu\text{m}$. The final patch dimensions were $54.17\ \text{mm} \times 54.17\ \text{mm}$. The antenna was gold plated in order to avoid oxidation of the copper and increase the lifetime and performance of the antenna.

The patch substrate was chosen for high radiation efficiency and large bandwidth. The final choice was Rogers 4003 with a thickness of 60 mils (1.524 mm), dielectric constant of 3.38 and loss tangent of 0.0027. The dielectric constant and thickness of the substrate material were also very critical to allow for a proper resonance frequency. For this reason, the material had to be very reliable. Also, the low-loss properties of this material allowed for efficient radiation. The patch substrate dimensions were $85\ \text{mm} \times 85\ \text{mm}$.

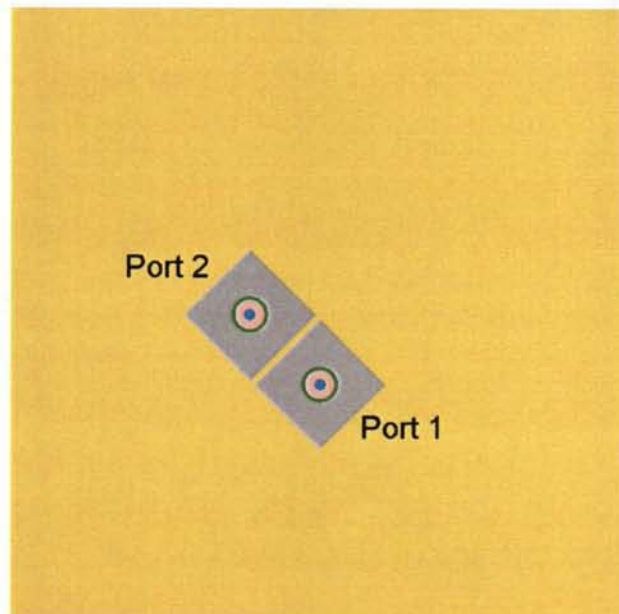
Figure 3 shows photographs of the patch antenna etched on the substrate. The holes in the patch were used for probe feeding. The holes along the side were used for assembly. Note that the metallization was removed from the back of the substrate. Appendix A shows a technical drawing of the substrate and patch.

2.2.2. Lexan frame and air substrate

A Lexan frame was used to create an air gap between the patch substrate and the ground plane. The air gap increased the bandwidth of the antenna. The thickness of the air gap and Lexan frame was 2.5 mm. The outer dimension of the frame was $85\ \text{mm} \times 85\ \text{mm}$. Lexan was used because of its low dielectric constant (2.56) and mechanical properties. The walls of the frame were narrow



a



b

Figure 2: Schematic representation of the MIMO antenna (approximately to scale) a. top view (showing frame underneath patch substrate); b. bottom view.

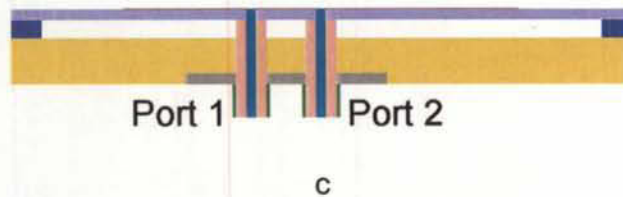










Figure 2 (continued): c. side view (cross-section).

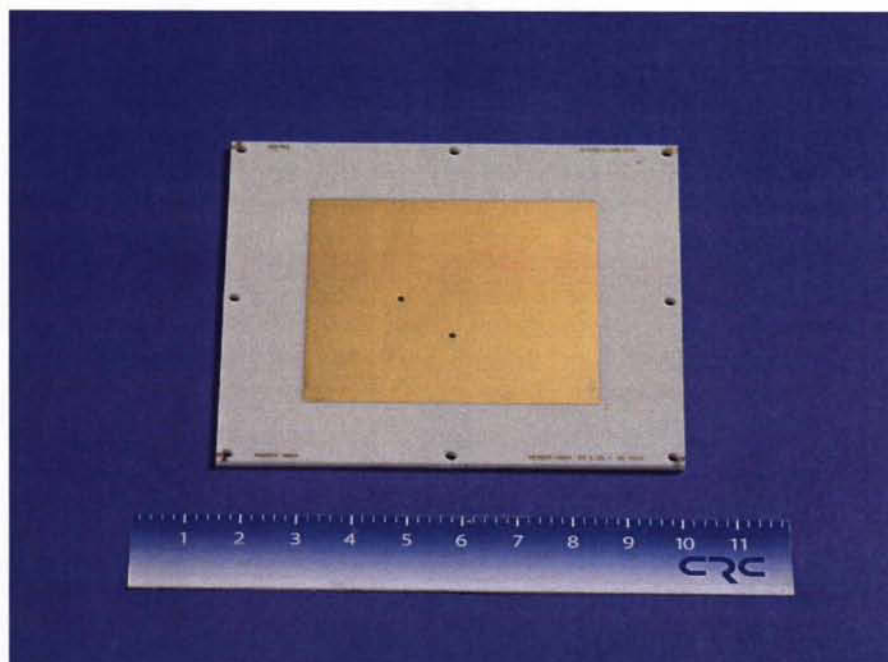
Table I: Color legend for Figure 2.

Color	Antenna part
	Metal patch antenna
	Probe / coaxial inner conductor
	Patch substrate
	Lexan frame
	Aluminum plate / ground plane
	Coaxial port / outer conductor
	Coaxial dielectric material
	Coaxial port flange
	Air

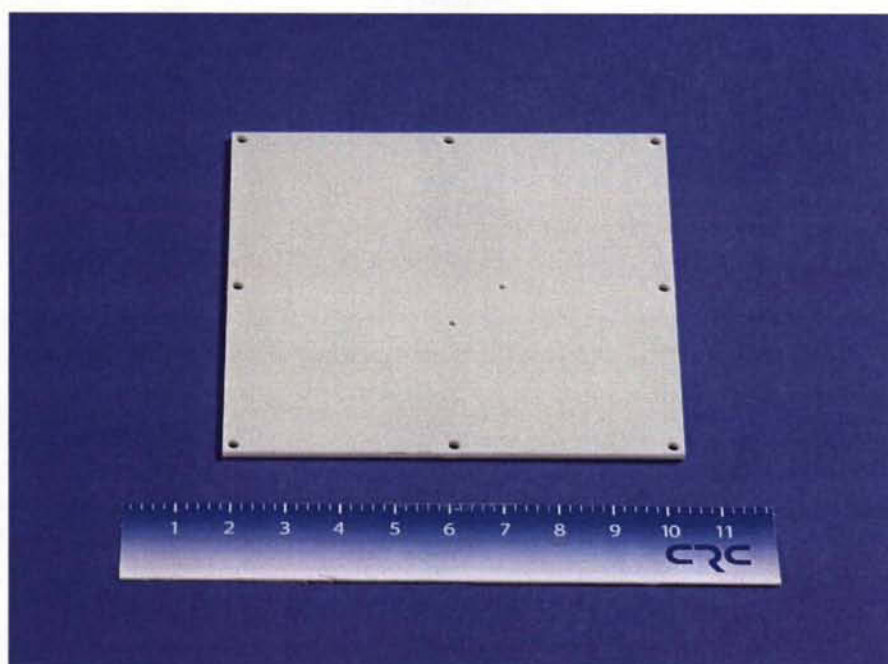
so they would not be under the patch and therefore not influence the electrical performance. Figure 4 shows a photograph of the Lexan frame. Appendix A shows a technical drawing of the Lexan frame.

2.2.3. Thick ground plane

To increase the mechanical strength of the antenna and to allow for robust assembly of the connectors, a 6.35 mm thick aluminium plate was used for the ground plane. Aluminium was chosen for robustness, light weight and low corrosion. To further reduce corrosion, the aluminium plate was also gold chromated.



a



b

Figure 3: The patch antenna etched on its substrate a. front view; b. back view (units on ruler are centimetres).

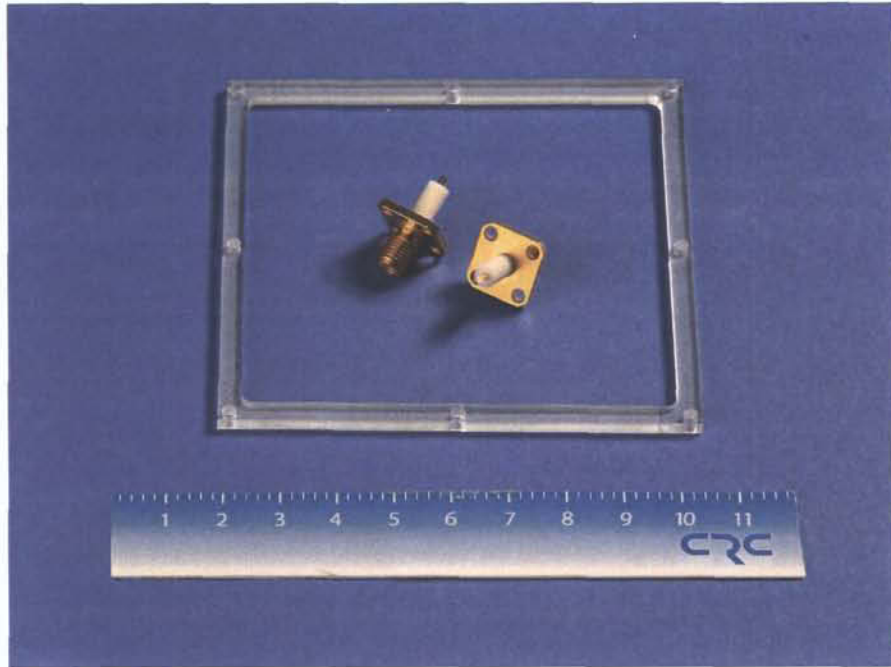


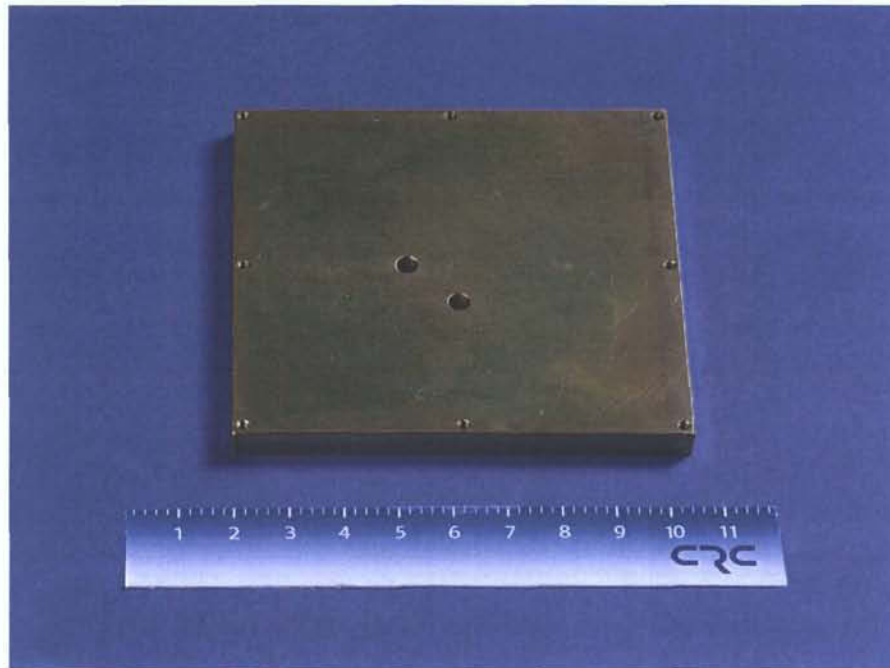
Figure 4: Lexan frame and SMA connectors (units on ruler are centimetres).

Figure 5 shows the thick ground plane aluminium plate. The top view shows two holes used to fit the coaxial extension of the connectors, i.e. dielectric and inner conductor (while the aluminium plate acts as the outer conductor). The bottom view shows the same two holes in addition with grooves to fit the connectors and ensure better mechanical robustness. Appendix A shows a technical drawing of the thick ground plane aluminium plate.

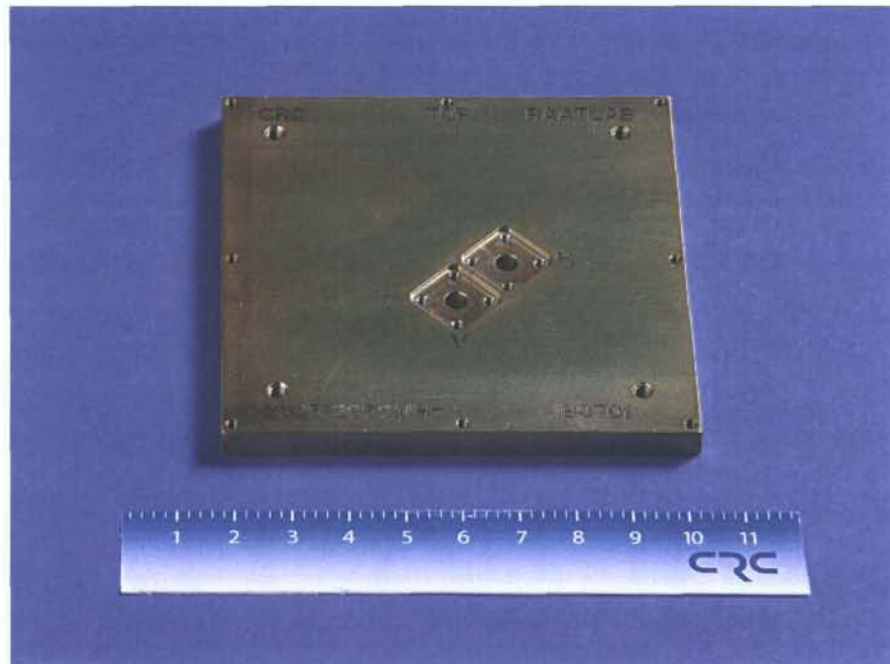
2.2.4. Connectors and probes

Two connectors were used in order to obtain vertical and horizontal polarizations. These connectors were 50 Ω coaxial SMA type with Teflon dielectric material used between the inner and outer conductors as insulator. The diameter of the inner conductor was 1.27 mm and the diameter of the outer conductor – i.e. the diameter of the hole in the aluminium plate – was 4.1 mm. These dimensions allowed for 50 Ω impedance. Figure 4 shows the connectors.

The connectors were made long in order to directly feed the patches. The Teflon insulator was used in the thick ground plane and frame/air layers; it was removed for the patch substrate layer in order to probe feed the patch antenna. Note that having the Teflon insulator extending in the air layer was unusual; however it guaranteed an additional mechanical support for the patch substrate without significant influence on the antenna performance since the dielectric



a



b

Figure 5: The thick ground plane aluminium plate a. top view; b. bottom view (units on ruler are centimetres).

constant of Teflon was low. Appendix A shows a technical drawing of a connector.

To guarantee an electric contact between the probes and patch and to facilitate soldering, the probes were made slightly longer so that they were slightly higher compared to the patch.

2.3. Antenna Assembly

The antenna was then assembled using the components presented in the previous section. The following subsections describe the assembly steps.

2.3.1. Connector installation

The first step consisted of installing the connectors to the thick ground plane aluminium plate. This was done by inserting the connectors in the grooves and screwing them into place. Figure 6 shows the completion of this step. It is seen that the Teflon section is extended, as described in Section 2.2.4.

2.3.2. Frame installation

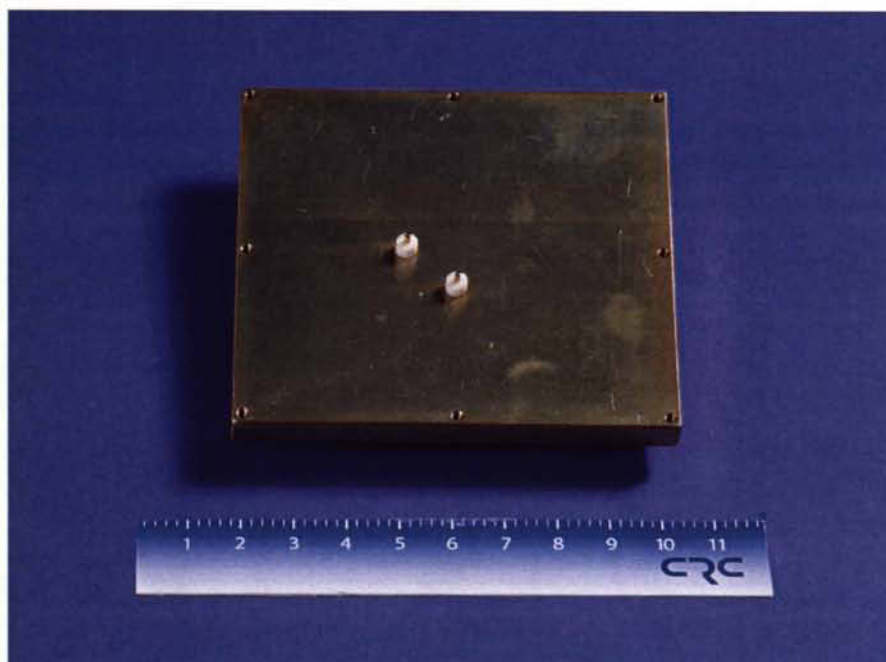
The next step consisted in placing the Lexan frame on top of the thick ground plane aluminium plate. The frame was not screwed but was sandwiched between the aluminium plate and the antenna substrate. Figure 7 shows the completion of this step.

2.3.3. Antenna substrate installation

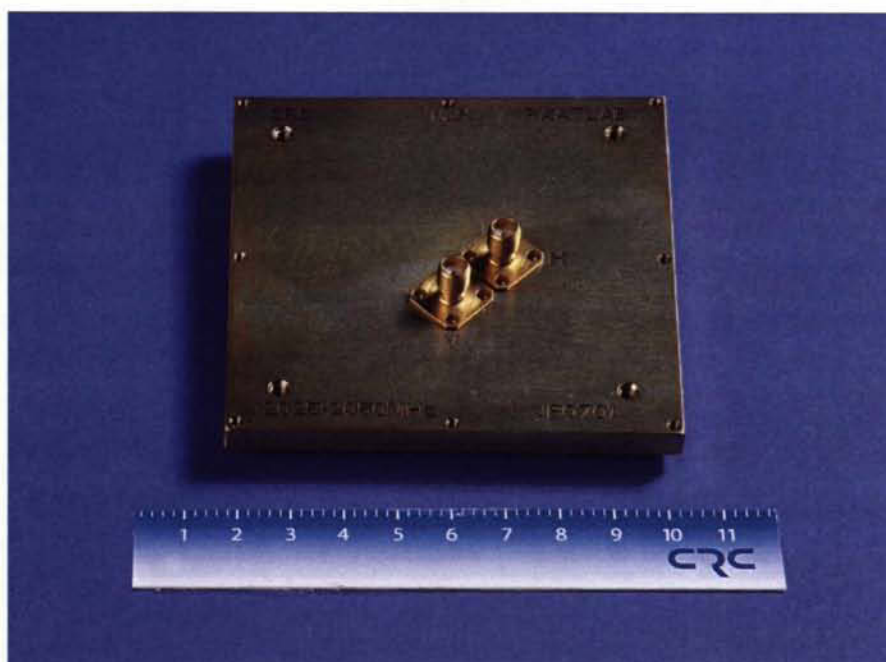
The following step consisted of installing the antenna substrate on top of the Lexan frame. The probes and holes had to be aligned for the antenna substrate to fit properly onto the frame. The antenna substrate was then screwed to the ground plane plate through the Lexan frame using nylon screws, which are less inclined to influence the electrical performance of the antenna than metal screws.

2.3.4. Probe soldering

The final step consisted in soldering the probes to the patch antenna. Figure 8 shows the antenna once fully assembled.



a



b

Figure 6: Installation of the connectors to the thick ground plane aluminium plate (screws not shown) a. top view; b. bottom view (units on ruler are centimetres).

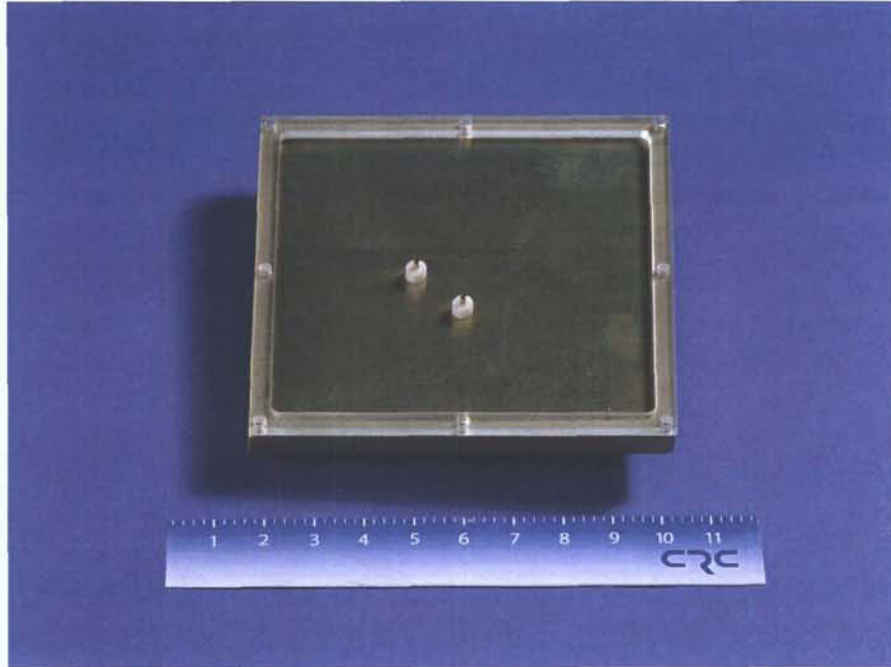
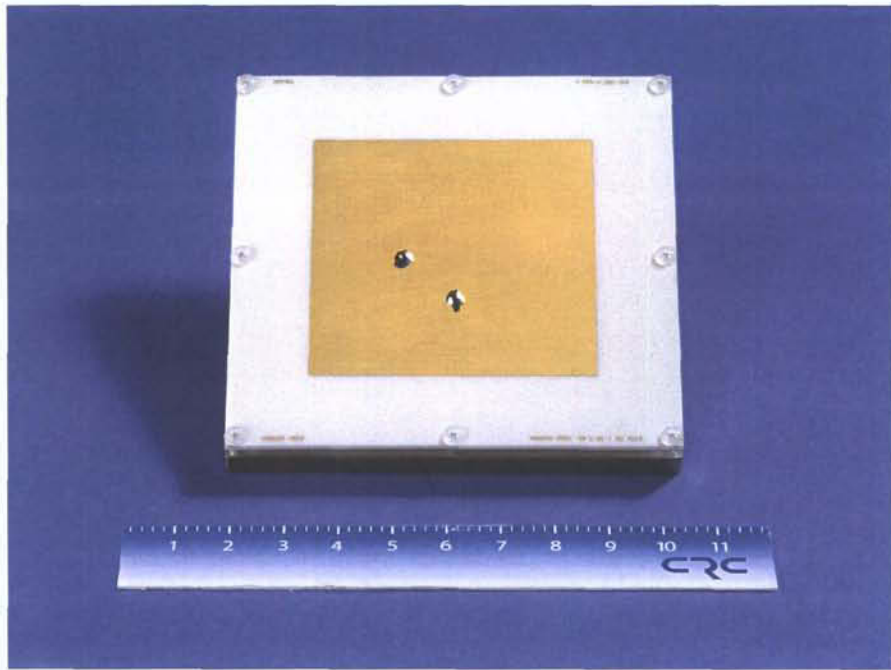
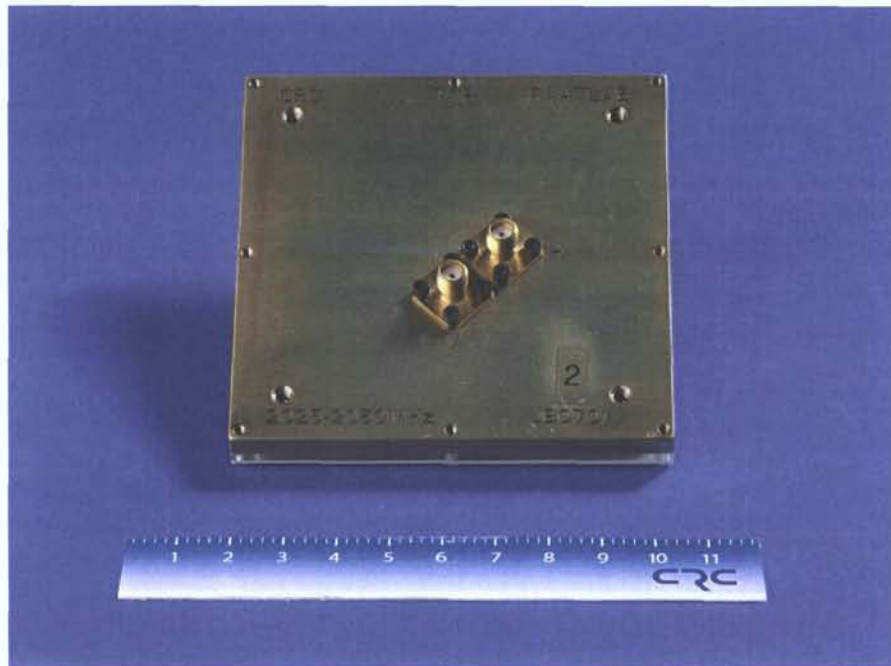


Figure 7: Installation of the Lexan frame (units on ruler are centimetres).



a



b

Figure 8: Fully-assembled antenna a. front view; b. back view (units on ruler are centimetres).

<This page intentionally left blank>

3. Results

Ten units of the antenna presented in the previous section were built and delivered to the Radio Communications Technologies (RRCT) group. One extra unit was built for the Advanced Antenna Technology (RAAT) group. The only difference between the RAATLab unit and the other units is that the RAATLab unit was not gold plated. Note that the gold plating is not expected to affect the results.

3.1 Scattering Parameters

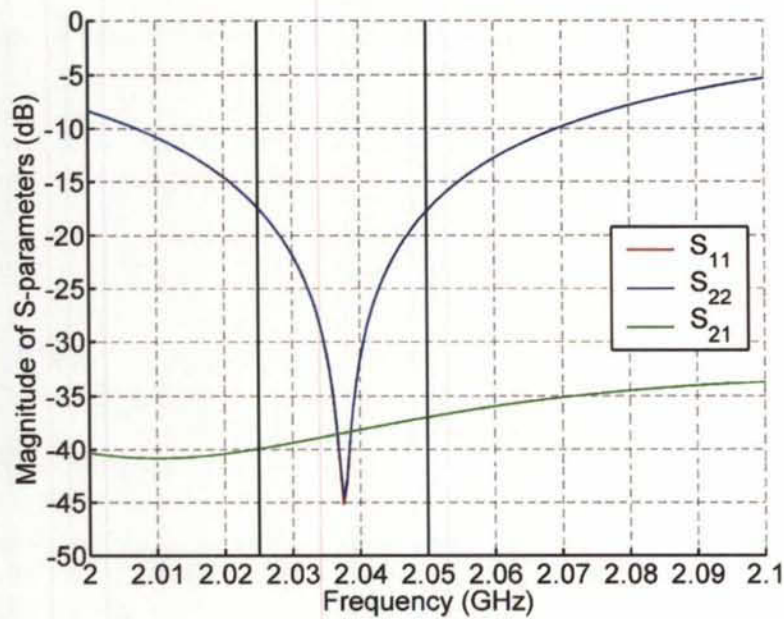
The simulated and measured scattering parameters of the MIMO antenna are presented in Figure 9. The simulations were performed in Empire™ XCcel, a finite-difference time-domain (FDTD) simulation package [2]. The measured results are for the RAATLab antenna. From Figure 9, good agreement is observed despite the slight shift in frequency. The 10 dB level for the return loss is in very close agreement when comparing simulation and measurement. Even at the 15 dB level, the agreement remains fairly close. As for the isolation between the ports (S_{21}), the level is in the same range for both simulation and measurement despite the numerous fluctuations observed for the measured results.

The scattering parameters of all the MIMO antennas fabricated were measured. The results are presented in Appendix B. It is observed that the return loss is better than 15 dB and the isolation better than 30 dB in the operating band. Note that for all the cases, including Figure 9, port 1 corresponds to vertical polarization (V) and port 2 corresponds to horizontal polarization (H).

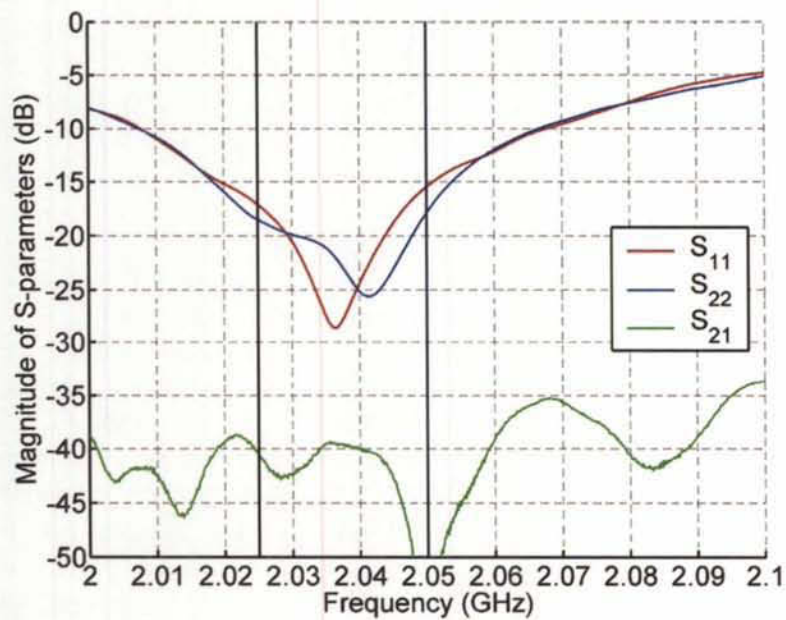
3.2 Radiation Patterns

The far-field radiation patterns of the MIMO antenna were simulated in Empire™ XCcel [2] and measured in RAATLab's far-field anechoic chamber. A specifically-designed plastic mount was used to measure the antenna, as shown in Figure 10. Plastic was chosen rather than metal in order to minimize the influence on the antenna during the measurement process. However, metal posts and a metal plate were used behind the antenna for better mechanical strength, as shown in Figure 11. The antenna was then mounted on the tower of the anechoic chamber, as shown in Figure 12. Absorber sheets were placed on the metal plate and around the metal posts in order to minimize the influence during the measurement process, as shown in Figures 12 and 13.

The simulated and measured far-field radiation patterns are presented for one case in Figure 14. The gain and beam shape are in very good agreement. The cross-polarisation (X-pol) patterns are different, showing higher levels for the

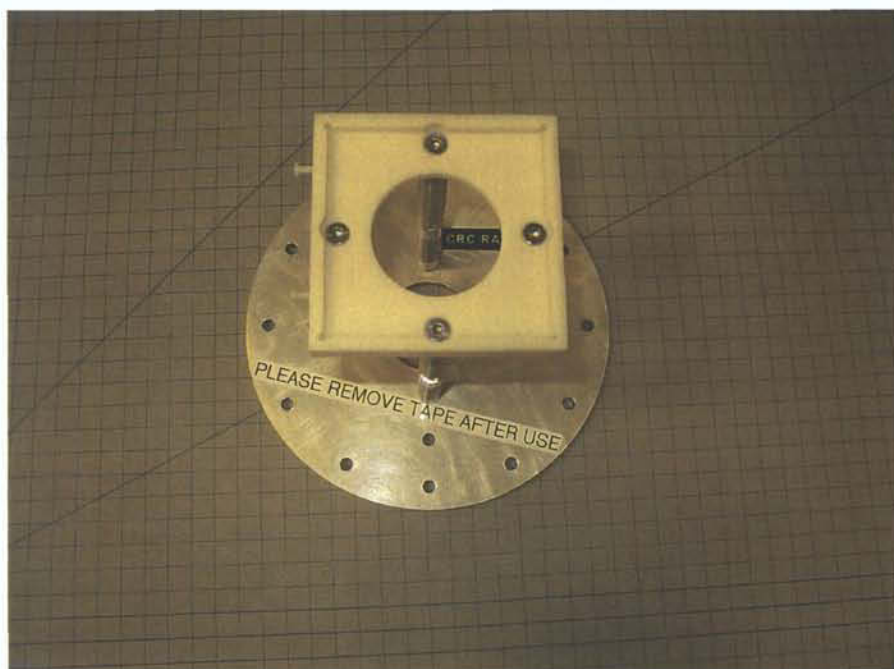


a

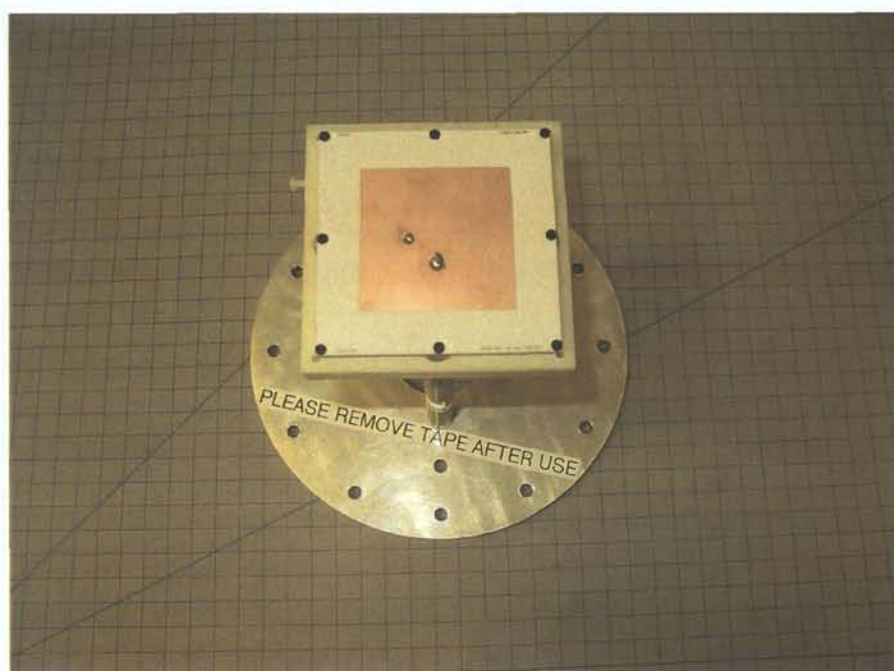


b

Figure 9: Scattering parameters of the MIMO antenna (RAATLab unit) a. simulated; b. measured.

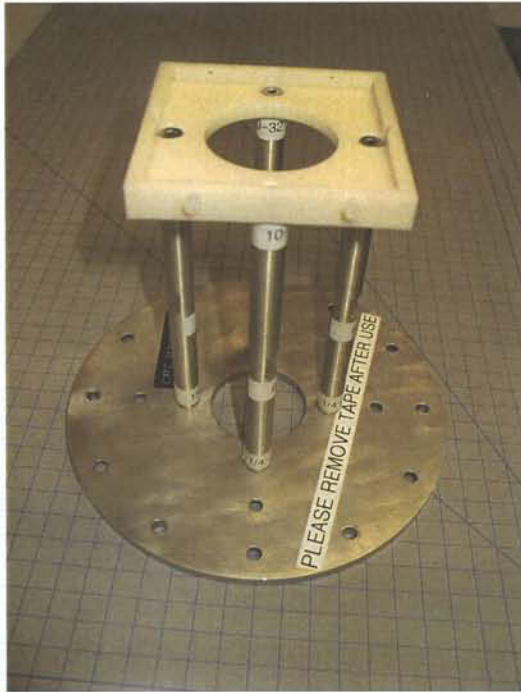


a

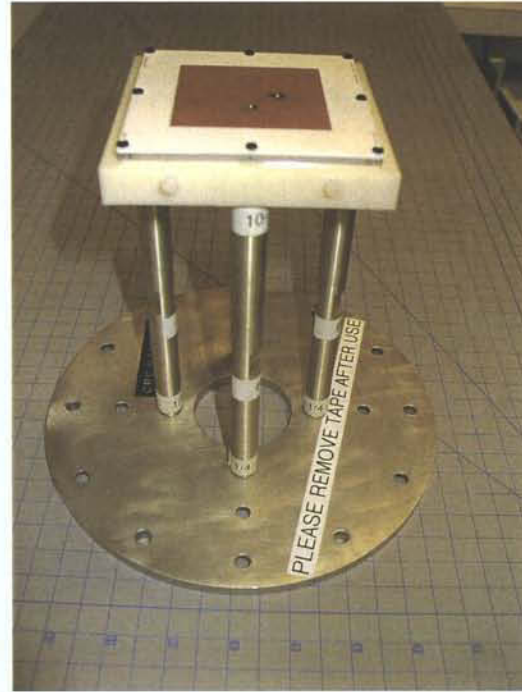


b

Figure 10: Front view of the mount used in the far-field anechoic chamber
a. without antenna; b. with antenna.



a

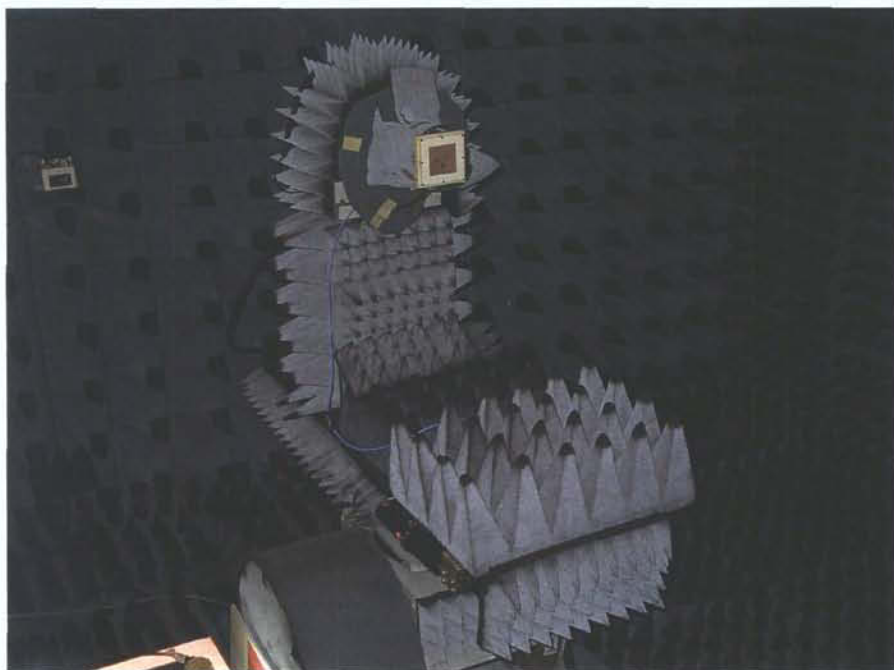


b

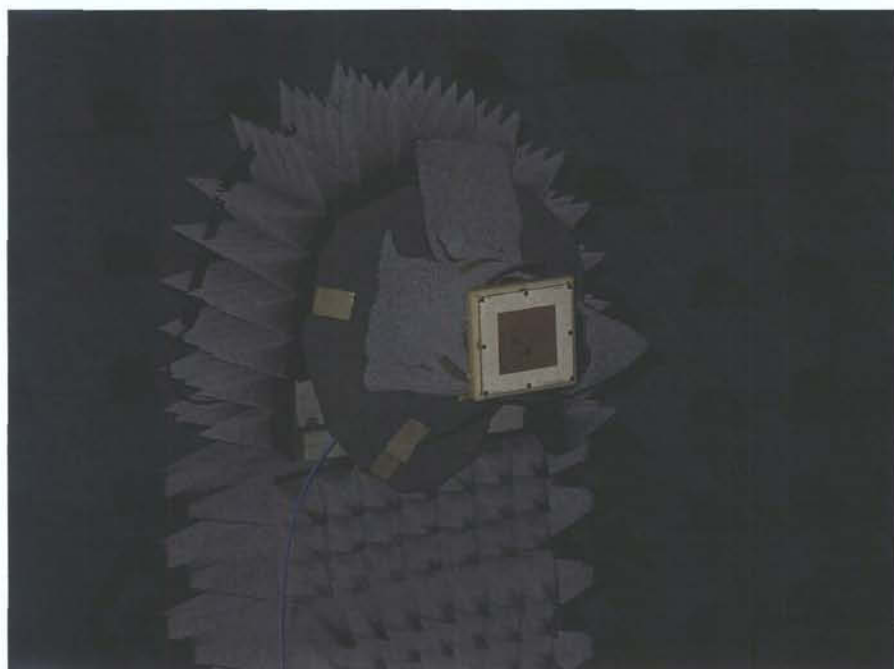
Figure 11: Side view of the mount used in the far-field anechoic chamber a. without antenna; b. with antenna.

measurement results. This can be explained by the measurement setup, including the presence of metallic parts near the antenna, tower, etc. For the measurement, the X-pol component is typically 18 dB below the co-pol component, which should be sufficient for this type of application. Appendix C presents the far-field results for both ports at three different frequencies in the operation band: 2.025 GHz (lower band), 2.0375 GHz (mid band) and 2.050 GHz (upper band). These results are for the RAATLab antenna. The radiation patterns of other antennas were not measured because of time constraints. However, it is believed that the radiation patterns will be in agreement with those presented in Appendix C.

Figure 15 presents the measured gain of the RAATLab antenna with respect to frequency for both ports. It is shown that the gain was almost identical for each port. Also, the gain was fairly constant within the operating band, ranging from 8 dBi to 9 dBi.



a



b

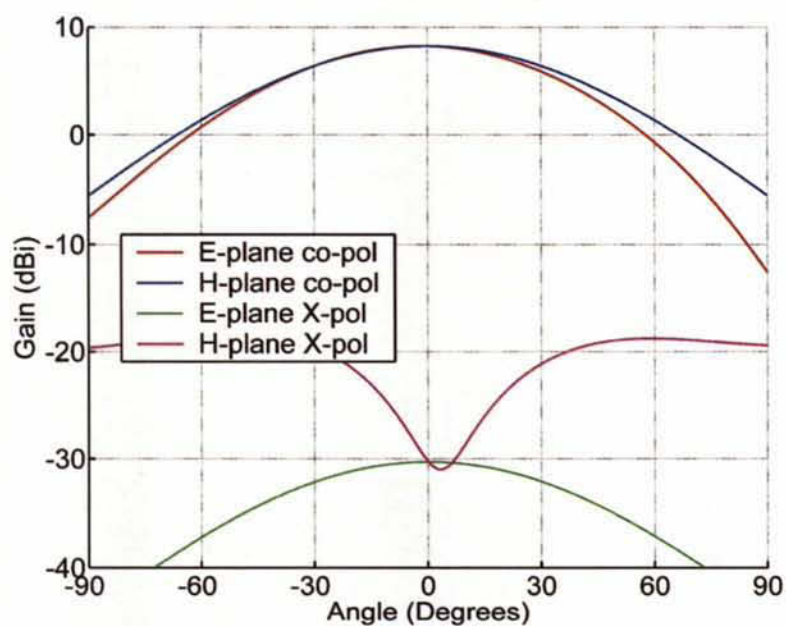
Figure 12: Tower of the far-field anechoic chamber with MIMO antenna (RAATLab unit) a. full view; b. close view.



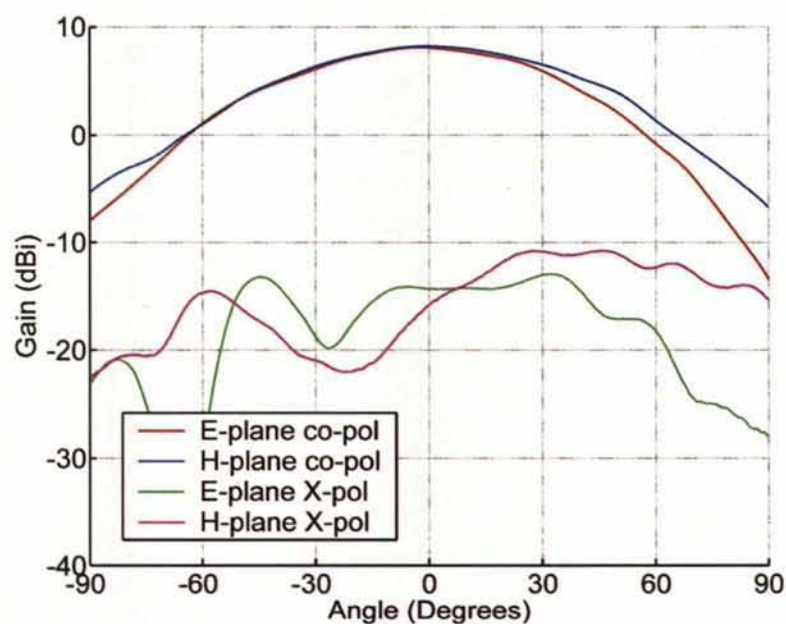
Figure 13: MIMO antenna mounted on the tower of the far-field chamber showing absorbing material covering the metal plate and posts.

3.3 Conclusions

The simulated and measured results were in very good agreement for the S-parameters and the radiation patterns. The performances obtained by this antenna met the required specifications. Table II summarizes the results.



a



b

Figure 14: Far-field radiation patterns of the MIMO antenna (RAATLab unit) for vertical polarization (port 1) at lower frequency (2.025 GHz) a. simulated; b. measured.

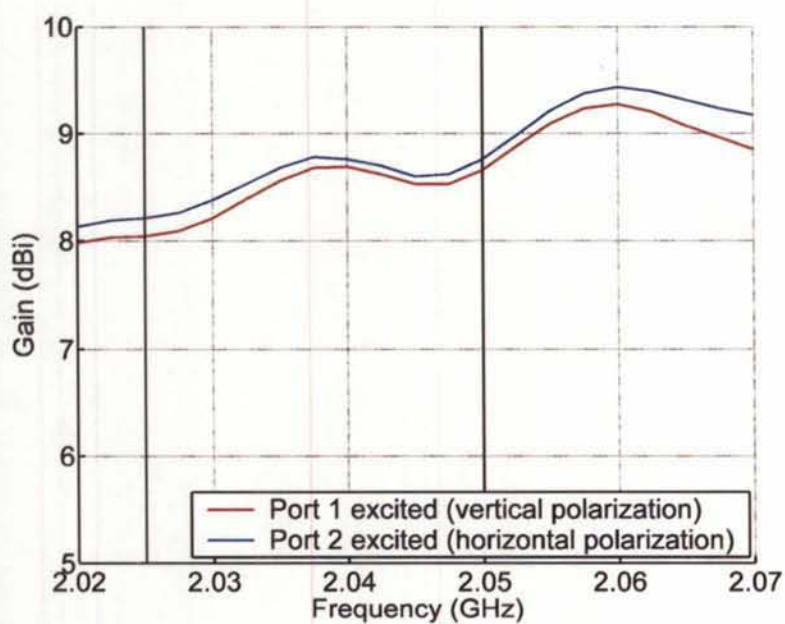


Figure 15: Measured gain versus frequency for the MIMO antenna (RAATLab unit).

Table II: Performances of the MIMO antenna.

	Min	Typical	Max	Unit
Return loss (worse case)	14	15	16	dB
Isolation (worse case)	29	35	40	dB
Antenna gain	8.0	8.5	8.8	dBi
E-plane 3 dB beam width	70	72	74	degrees
H-plane 3 dB beam width	78	80	83	degrees
E-plane 10 dB beam width	133	134	—	degrees
H-plane 10 dB beam width	144	145	147	degrees
X-pol level (with respect to beam peak)	17	18	19	dB

4. Coupling Study

The coupling between antennas is a critical parameter that needs to be addressed in multiple antenna systems. It is usually desired that the coupling be as low as possible between antennas in order to minimize the influence of one antenna to another.

In order to verify the coupling between antennas, a special jig was built, as shown in Figure 16. This jig allowed for moving the antenna spacing along one axis and consequently for measuring the coupling between antennas as a function of spacing.

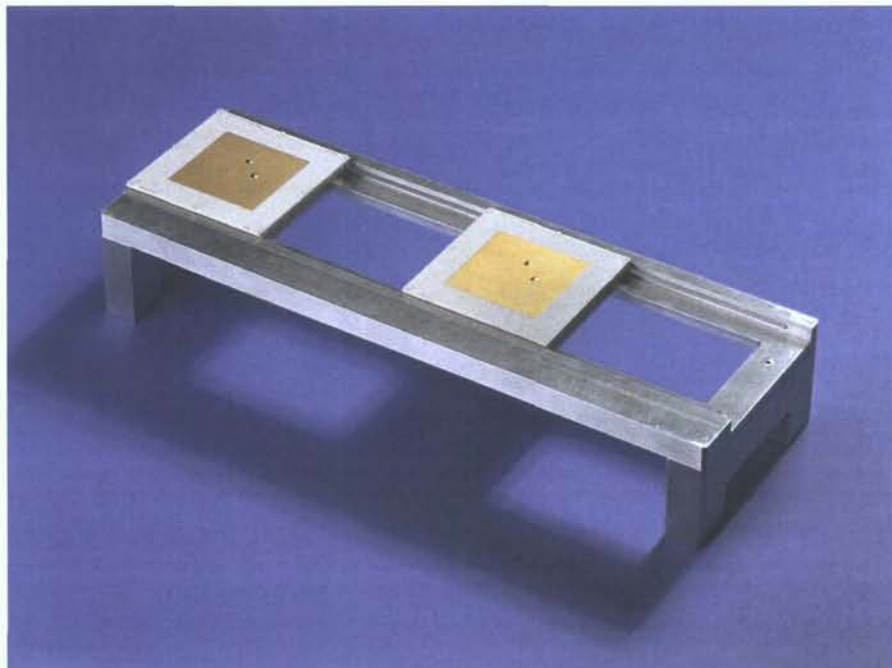


Figure 16: Two MIMO antennas on the special jig designed to measure the coupling.

The coupling between the different ports was measured using this approach. For this specific case, the ports were defined as follows:

- the port number referred to the antenna port, i.e. port 1 for vertical polarization and port 2 for horizontal polarization;
- the port letter referred to the antenna, i.e. A for the antenna on the left side and B for the antenna on the right side.

Figure 17 shows a schematic of the port definition as well as how the separation between the antennas was defined (i.e. centre to centre).

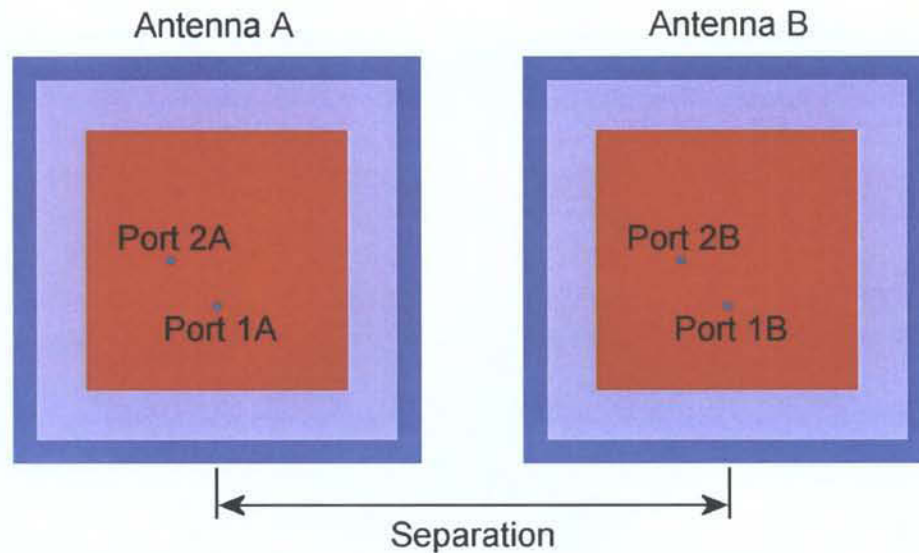


Figure 17: Schematic view of the coupling experiment including port and separation definitions.

The results of the coupling experiment are presented in Figure 18¹. As expected, the coupling was generally stronger when the antennas were close to each other. The 85 mm separation occurs when the two antennas are touching each other. The worst case coupling occurred between the two horizontally-polarized ports, i.e. between port 2A and port 2B, and the worst case value is approximately -15 dB. Also, the fact that the jig was made of metal could have contributed to the increased coupling.

During the coupling study, the return loss and isolation between the ports of the same antenna were also measured to verify if the presence of another antenna in the surroundings was affecting the results. It turned out that these parameters were not affected at all or only slightly modified, but not significantly. This was expected since the coupling from the other antenna was low, i.e. -15 dB or less.

¹ The results presented in Figure 18 are for an early prototype of the MIMO antenna, which is not described in this report for simplification. This prototype used the same substrate, frame and back plate; however the connectors and vias were different. Even though the electromagnetic performances of this antenna were good, the some part of the mechanical design was weak and needed revision. It is believed that the results presented in Figure 18 would be in very good agreement for the current MIMO antenna design and, for this reason, the coupling measurement were not reconducted.

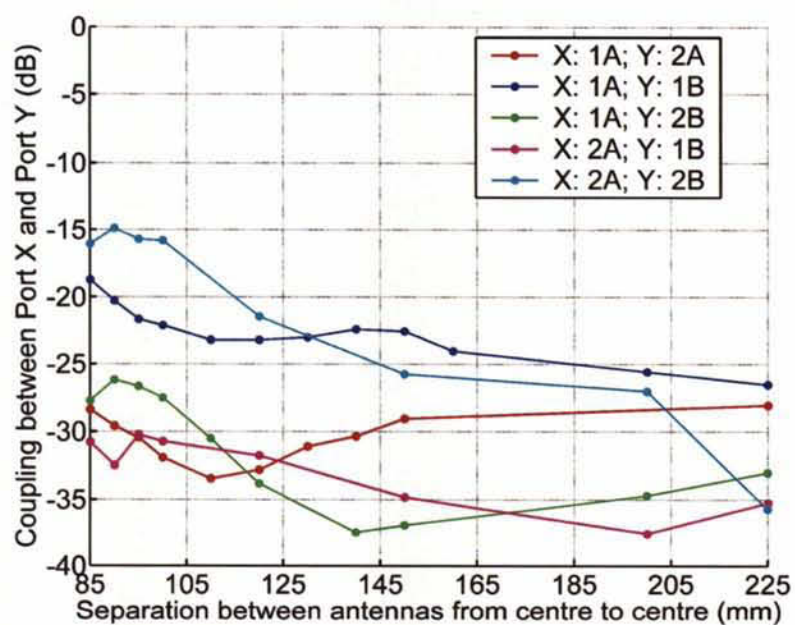


Figure 18: Coupling between ports as a function of distance (worst case coupling within operating band shown).

<This page intentionally left blank>

5. Simulations on Vehicle

The MIMO antennas are to be installed on a military vehicle. The military vehicle to be used is a LAV (Land Assault Vehicle) III, as shown in Figure 19. A computer-aided design (CAD) model of this vehicle was obtained in order to simulate the radiation patterns of the MIMO antenna when mounted on various locations of the LAV III. The model was modified and used in our simulation software Empire™ XCcel from IMST [2]. The model used is shown in Figure 20. It was a filled, all-metal model in order to reduce the memory requirements during simulations.



Figure 19: A LAV III from the Canadian forces (Photo: Department of National Defence).

5.1 MIMO antenna simplified model

The main problem in performing simulations of microwave antennas on vehicles is the large memory requirements. To fit within the memory constraints a coarser meshing of the structure was necessary, therefore the antenna cannot be meshed as densely as if the antenna were simulated on its own. In this particular case, the interest was to look at the effect of the radiation patterns when the antenna was mounted on a LAV III (the effect on the antenna input impedance was deemed to be small). Prior to performing antenna-on-vehicle simulations, the antenna alone was simulated and the mesh density was reduced

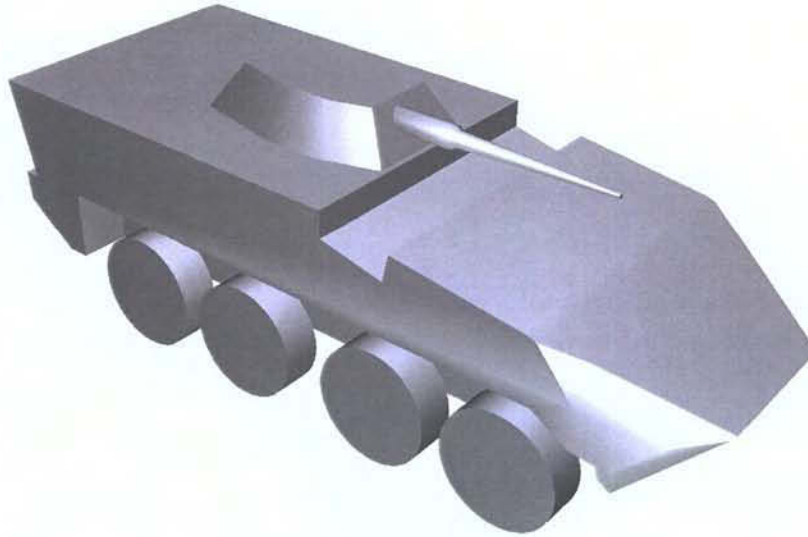


Figure 20: The LAV III model used for simulation.

as much as possible in order for the antenna to produce similar radiation patterns as the densely-meshed case. This allowed for the computer memory to support the problem. It was found that the mesh density had a greater effect on the S-parameters while the radiation patterns remained very similar even though the meshing density was significantly reduced.

To further reduce the memory requirements, the coaxial ports and probes were modified from circular to square to accommodate the rectangular meshing used by the software. The discretization data are shown in Table III for both the initial case (densely-meshed case) and the modified case. Figure 21 and Figure 22 show the simulated S-parameters and far-field radiation patterns of the modified case, respectively. The S-parameters of the simplified model are not as good as those of the initial model (see Figure 9); however they are more than acceptable with a return loss level in the operation band better than 15 dB and an isolation in the range between 25 and 30 dB (as opposed to a range of 30 dB to 35 dB for the initial model). As for the radiation patterns, the co-polarization patterns are almost identical (see Figure 14 for the initial model) despite a slightly lower gain and higher cross-polarization components for the simplified model. Consequently, the simplified model seemed to be adequate for use on a vehicle to verify the influence on the radiation patterns.

Table III: Discretization data for the two MIMO antenna simulation cases.

Direction	Information	Initial model	Simplified model
x	Number of mesh lines	425	25
	Min / Max subdivision (μm)	10 / 500.2	250 / 15000
y	Number of mesh lines	425	25
	Min / Max subdivision (μm)	10 / 500.2	250 / 15000
z	Number of mesh lines	91	9
	Min / Max subdivision (μm)	152.4 / 550.8	1574.8 / 5000

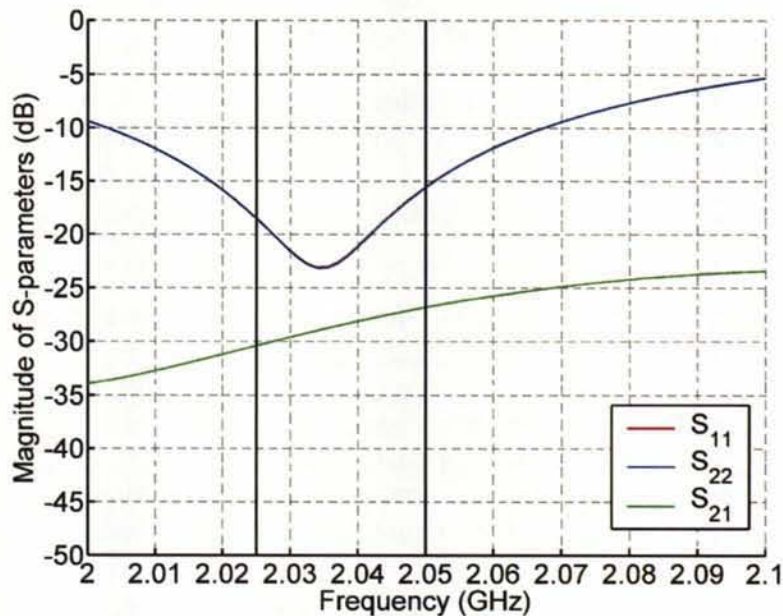


Figure 21: Scattering parameters of the simplified MIMO antenna model.

5.2 MIMO antenna on vehicle simulations

The MIMO antenna simplified model was then placed on different locations on the LAV III model to examine the influence of the vehicle structure on the radiation patterns. In these simulations, the LAV III was assumed to be a solid metal object and was the only structure in the simulation environment,

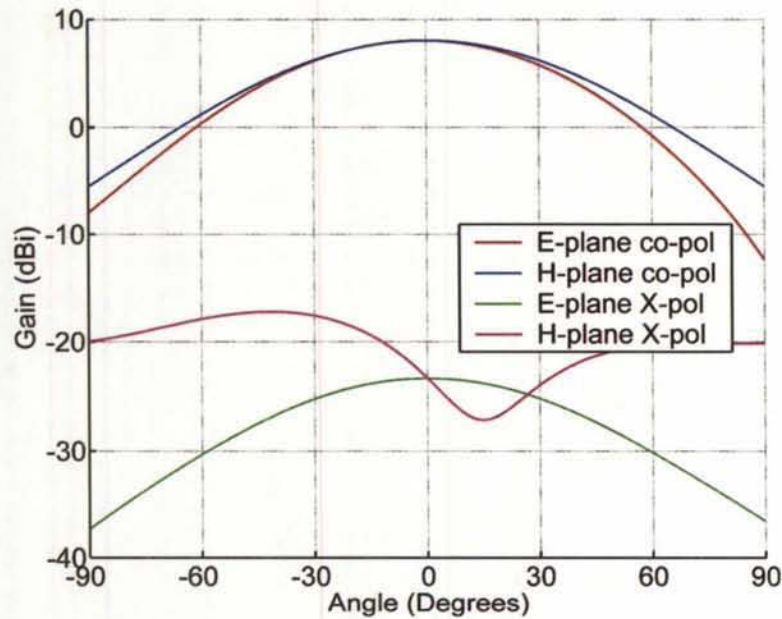


Figure 22: Simulated far-field radiation patterns of the simplified MIMO antenna for vertical polarization (port 1) at lower frequency (2.025 GHz).

surrounded by free-space. Consequently, no physical ground was used in the simulations, except if otherwise mentioned.

The MIMO antenna was placed at three different locations on the LAV III: on the top of the tower, centred on the back shell and on the side between the second and third wheels. Table IV provides a description of the figures presented in this subsection, showing antenna positions and radiation patterns. Note that the MIMO antenna's port 1, used in the far-field radiation patterns, is polarized along the y axis and propagating in the positive z direction for all cases. The coordinate system is displayed on the figures showing 3D views.

Table IV: Figure description for MIMO antenna mounted on a LAV III.

Position	Figure showing position	Figure showing 3D radiation	Figure showing radiation patterns
Top of the tower	Figure 23	Figure 24	Figure 25
Back of the shell	Figure 26	Figure 27	Figure 28
Side of the shell	Figure 29	Figure 30	Figure 31

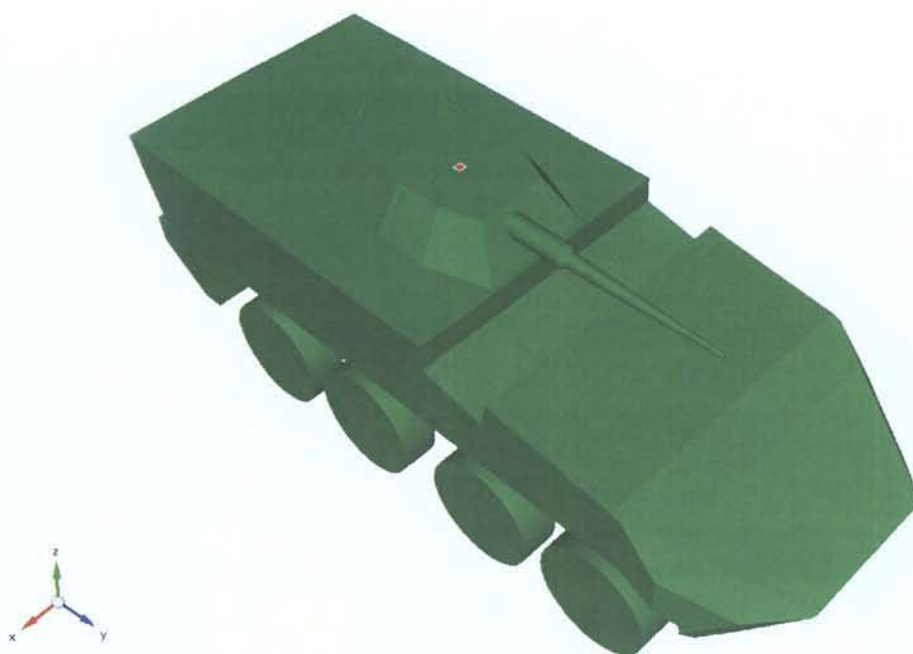


Figure 23: Empire™ 3D view of the LAV III model with MIMO antenna on top of the tower.

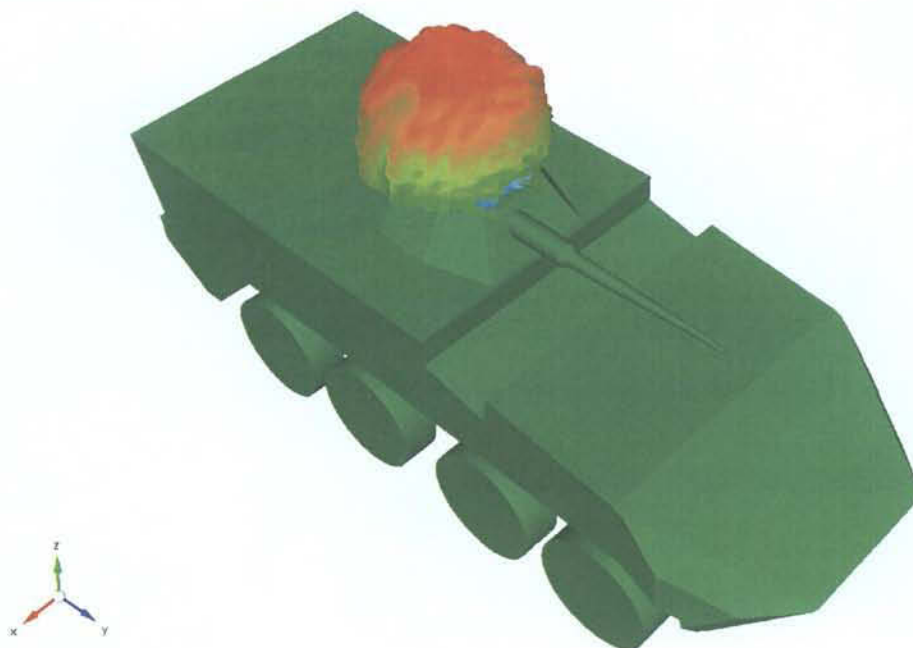


Figure 24: Empire™ 3D view of the LAV III model showing 3D far-field radiation pattern of the MIMO antenna on top of the tower.

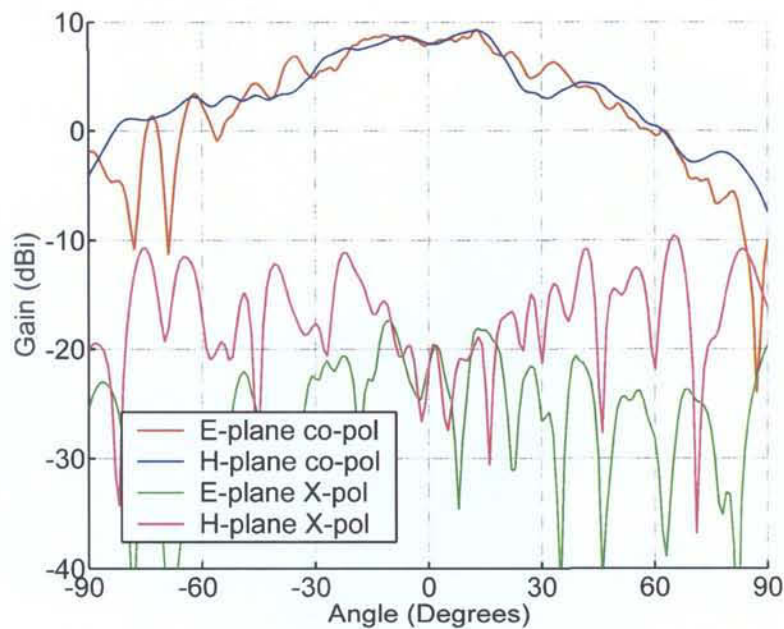


Figure 25: Simulated far-field radiation patterns of the simplified MIMO antenna for vertical polarization (port 1) at lower frequency (2.025 GHz) on top of the LAV III tower.

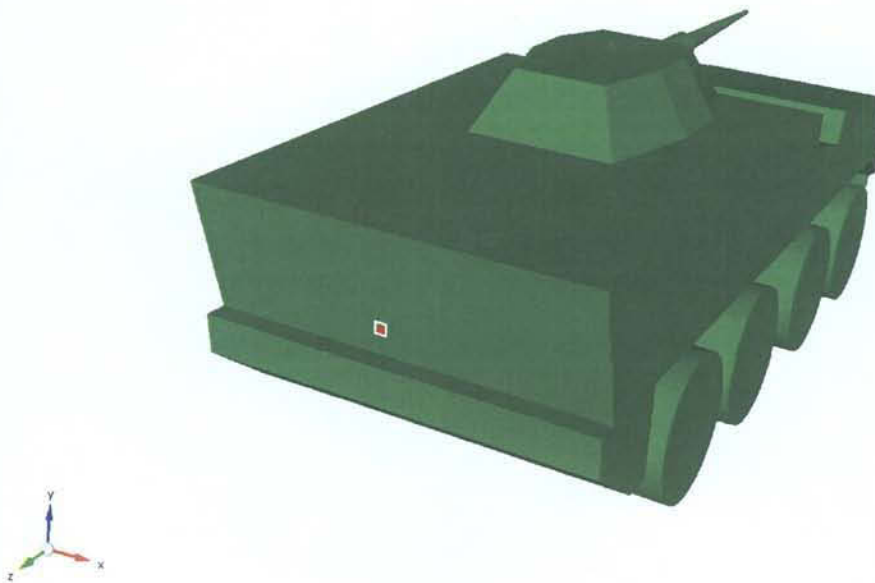


Figure 26: Empire™ 3D view of the LAV III model with MIMO antenna on the back of the shell.

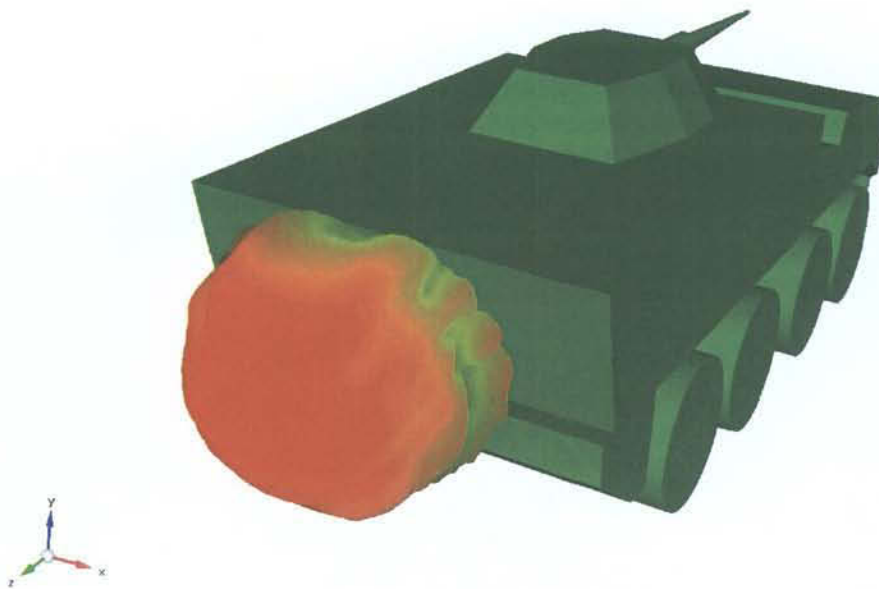


Figure 27: Empire™ 3D view of the LAV III model showing 3D far-field radiation pattern of the MIMO antenna on the back of the shell.

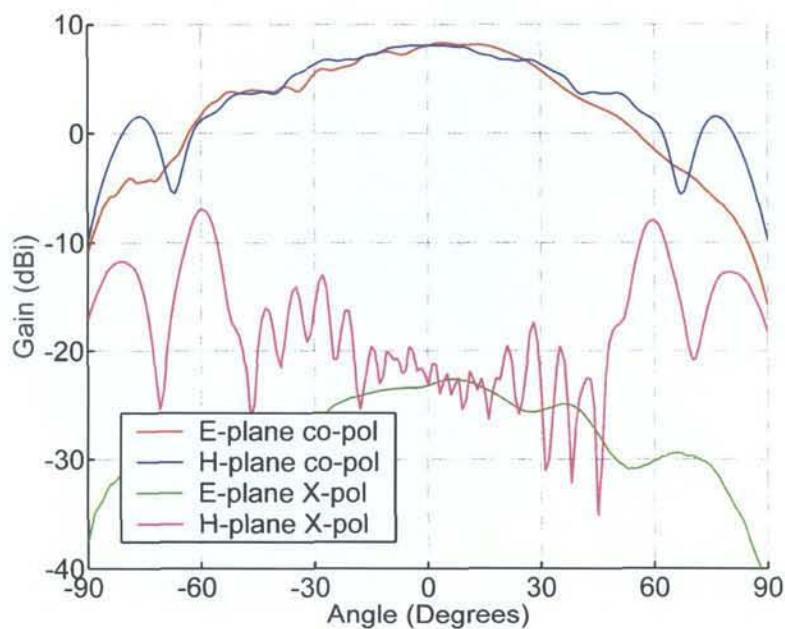


Figure 28: Simulated far-field radiation patterns of the simplified MIMO antenna for vertical polarization (port 1) at lower frequency (2.025 GHz) on the back of the LAV III.

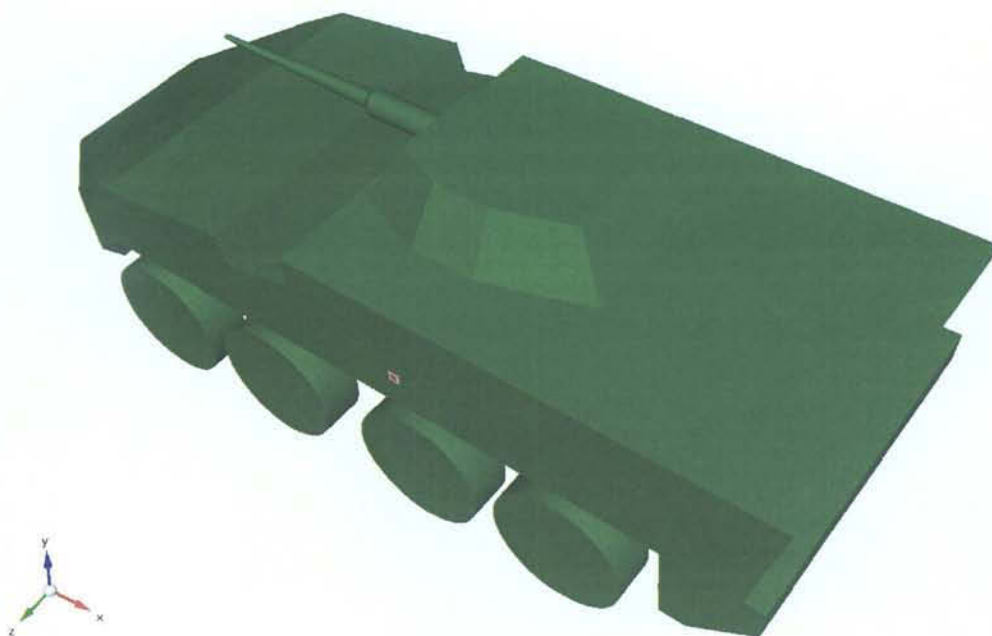


Figure 29: Empire™ 3D view of the LAV III model with MIMO antenna on the side of the shell.

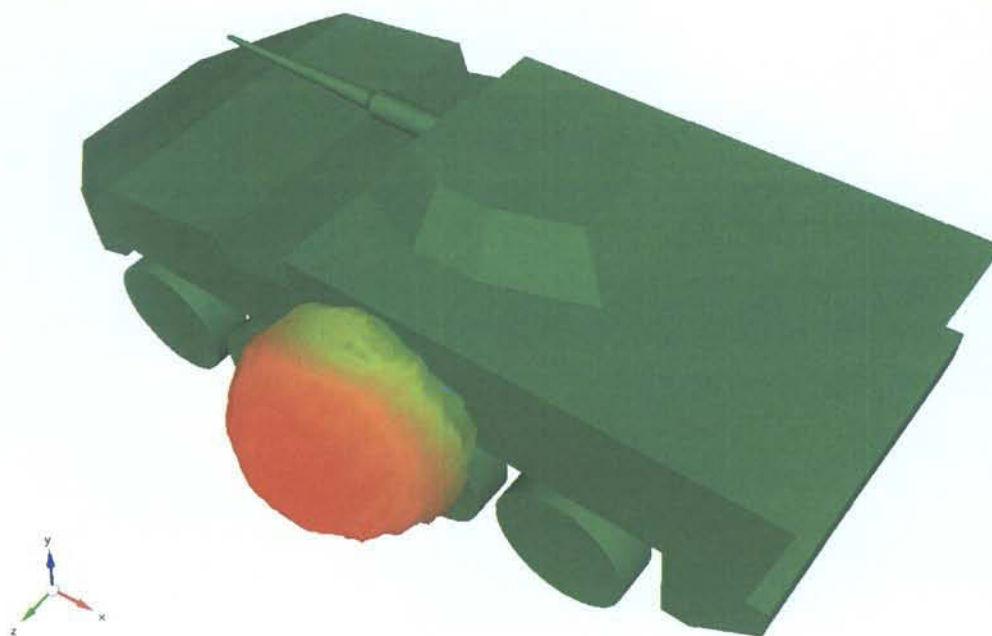


Figure 30: Empire™ 3D view of the LAV III model showing 3D far-field radiation pattern of the MIMO antenna on the side of the shell.

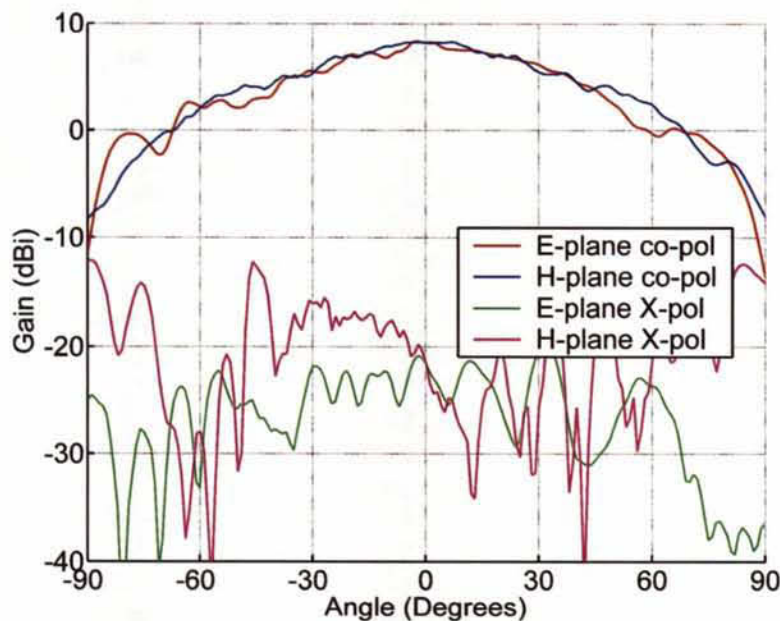


Figure 31: Simulated far-field radiation patterns of the simplified MIMO antenna for vertical polarization (port 1) at lower frequency (2.025 GHz) on the side of the LAV III.

By comparing the results of Figures 22, 25, 28 and 31, it is seen that the LAV III had an effect on the radiation patterns of the antenna. The most significant effects were:

- beam deformation, particularly near to broadside (see Figure 25);
- sidelobes near the end-fire direction (see Figure 28);
- rippled beam (see Figure 25, 28 and 31);
- higher level of cross-polarization components (see Figure 25, 28 and 31).

These effects were caused by the irregular shape of the LAV III, which acted as a scatterer.

5.2.1 Effect of meshing resolution on radiation patterns

The meshing of the structure is an important parameter. A denser mesh is more accurate, but it takes more time to run and it requires more computer memory. In this particular case, since the LAV III was a big structure, the resolution of the discretization had to be decreased in order to fit within the memory constraints. In order to verify the influence of the discretization on the structure, the case of the MIMO antenna on top of the LAV III tower was

simulated using three different meshing patterns. The description of the meshing patterns is summarized in Table V. Case 1 corresponds to the original case, presented in the previous section (see Figure 25); the radiation patterns for Cases 2 and 3 are shown in Figure 32 and 33, respectively. Note that the discretization in the MIMO antenna and its surroundings was the same for all cases: this is confirmed by the minimum subdivision values, shown in Table V, which are the same for all cases. Only the meshing of the vehicle itself was changing.

Table V: Discretization data for the three simulation cases of MIMO antenna on top of the tower.

Direction	Information	Case 1	Case 2	Case 3
x	Number of mesh lines	245	369	377
	Min subdivision (μm)	250	250	250
	Max subdivision (μm)	19954.55	15000	15000
y	Number of mesh lines	457	663	717
	Min subdivision (μm)	250	250	250
	Max subdivision (μm)	20029.07	15017.07	15000
z	Number of mesh lines	183	290	290
	Min subdivision (μm)	1574.8	1574.8	1574.8
	Max subdivision (μm)	20185.19	12495.82	12495.82
Number of cells		20489595	70947630	78389610

From these three cases, it is seen that the meshing had an influence on the radiation patterns. Cases 2 and 3, which had respectively about 3.5 times and 4 times more cells, had radiation patterns that were less deformed close to the main beam compared to Case 1. Comparison of the radiation patterns of Cases 2 and 3 showed that a convergence was almost reached since the co-polarization components presented many similarities; the cross-polarization components were more different, but they generally agreed.

Consequently, there is a trade-off in simulating such structures. The radiation patterns of Figure 25 for Case 1 appear to be worse than they should be in reality, but the structure can be simulated much faster than Cases 2 or 3.

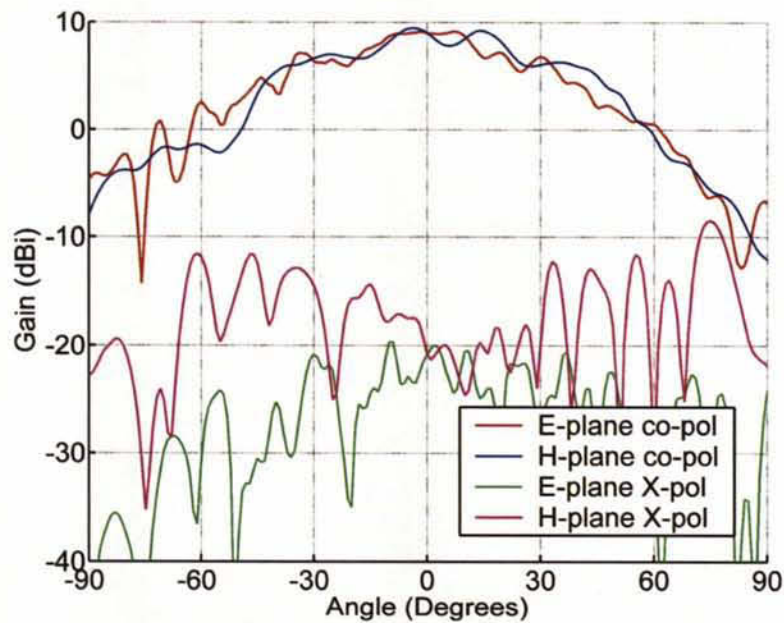


Figure 32: Simulated far-field radiation patterns of the simplified MIMO antenna for vertical polarization (port 1) at lower frequency (2.025 GHz) on top of the LAV III tower corresponding to Case 2 in Table V.

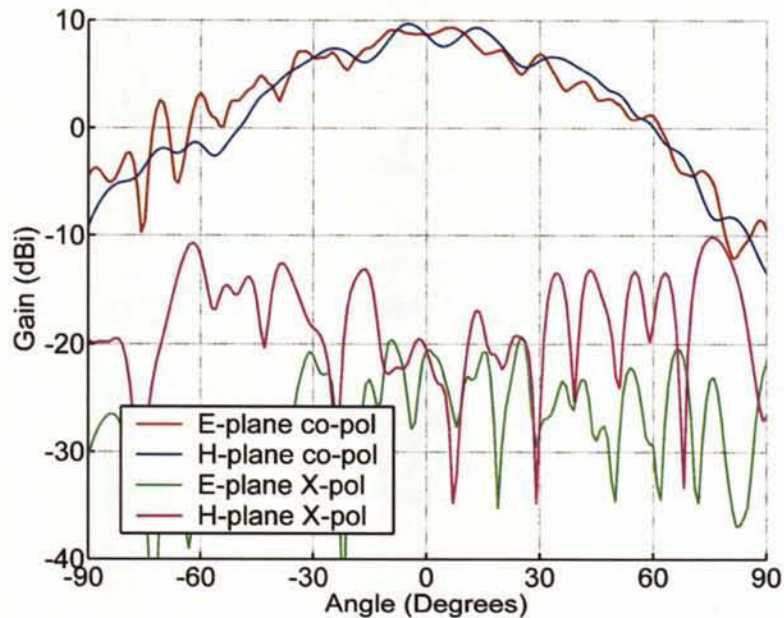


Figure 33: Simulated far-field radiation patterns of the simplified MIMO antenna for vertical polarization (port 1) at lower frequency (2.025 GHz) on top of the LAV III tower corresponding to Case 3 in Table V.

5.2.2 Effect of physical ground on radiation patterns

As mentioned previously, the physical ground was not included in the simulations. Consequently, these simulations are ideal case of a LAV III in a free-space environment without any surroundings.

In order to obtain a more realistic simulation, a ground was added in the simulation where the MIMO antenna was placed on the side of the LAV III shell. The ground was modeled as a simple perfectly conductive layer. The discretization was kept identical as the previous case. Figure 34 presents the radiation patterns for this case.

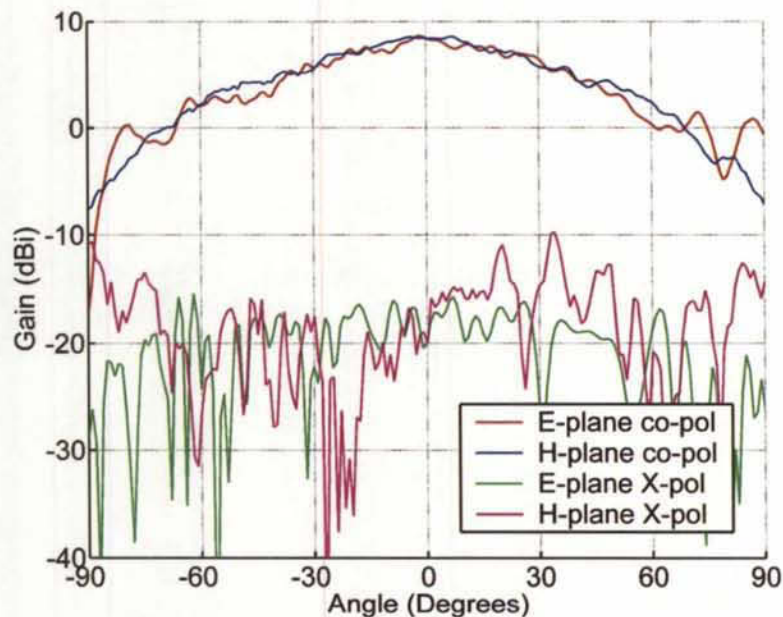


Figure 34: Simulated far-field radiation patterns of the simplified MIMO antenna for vertical polarization (port 1) at lower frequency (2.025 GHz) on the side of the LAV III with perfect electric conductive layer underneath.

A comparison between Figures 31 and 34 reveals that the ground, as it was modeled, does not present a significant impact on the radiation patterns for this case. The co-polarization patterns are almost identical, except near +90 degrees. However, the cross-polarization patterns are slightly increased, but their level is below -10 dB.

6 Conclusions

This document has described the design and fabrication of a probe-fed dual-port dual-polarized microstrip patch antenna to be used in multiple-input multiple-output (MIMO) communication systems. Scattering parameter and radiation pattern results revealed good performance of this antenna. An experimental coupling study, which confirmed relatively low coupling between two adjacent antennas, was conducted. Simulations of the antenna on a military vehicle were conducted to model the effect on the far-field radiation patterns. The major effects on the radiation patterns were ripples in the main beam, higher cross-polarization level, sidelobes near the end-fire direction and a slight beam deformation.

Ten units of the antenna were built for the Radio Communications Technologies (RRCT) group. A MIMO communication system using these antennas should then be set up and tested.

<This page intentionally left blank>

References

- [1] Angel Lozano, Farrokh R. Farrokhi, and Reinaldo A. Valenzuela, "Lifting the limits on high-speed wireless data access using antenna arrays," *IEEE Communications Magazine*, vol. 39, no. 9, pp. 156-162, September 2001.
- [2] IMST, Empire™ XCcel, <http://www.empire.de>

<This page intentionally left blank>

Appendix A: Technical Drawings

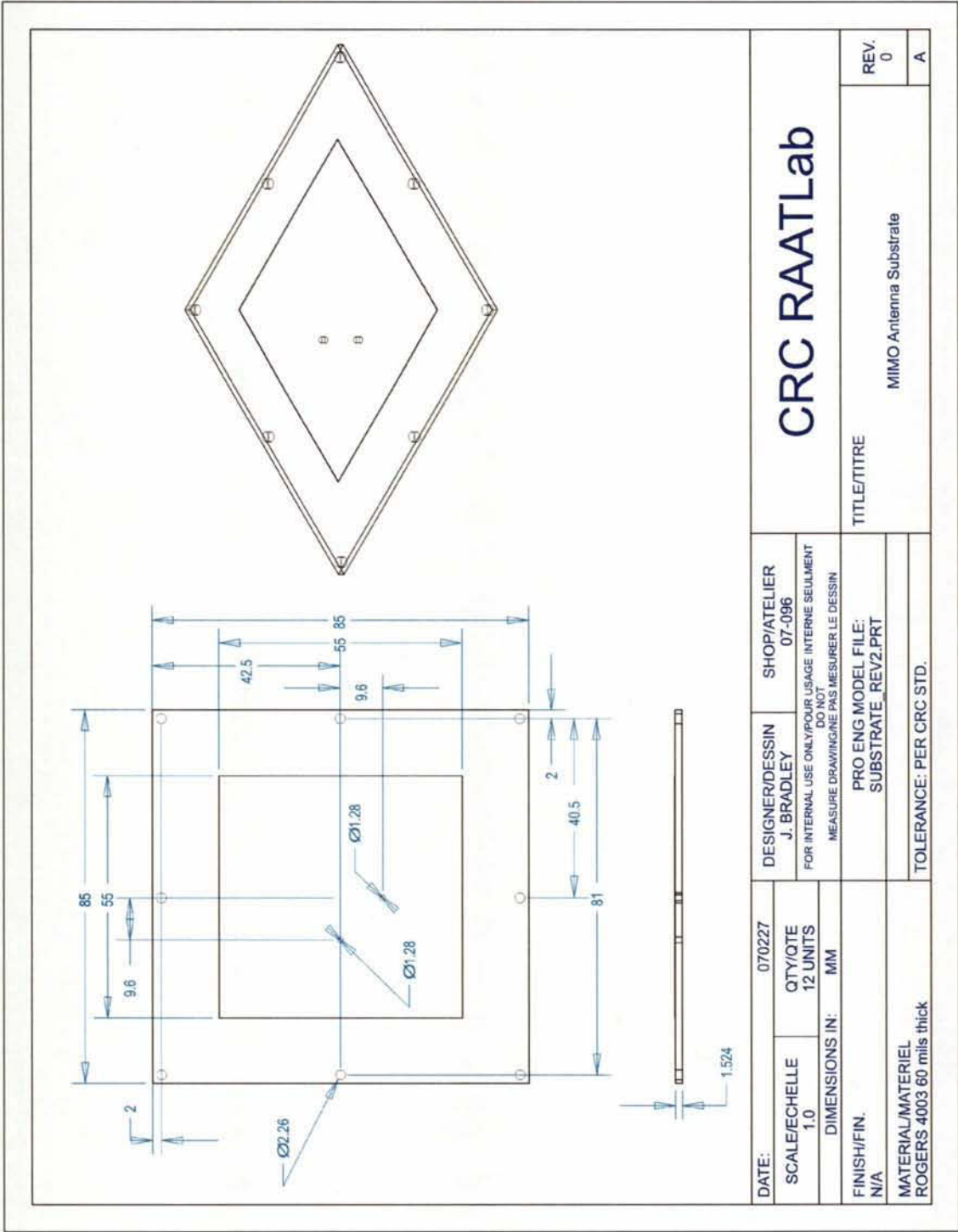


Figure 35: Patch and substrate technical drawing (approximate patch dimensions).

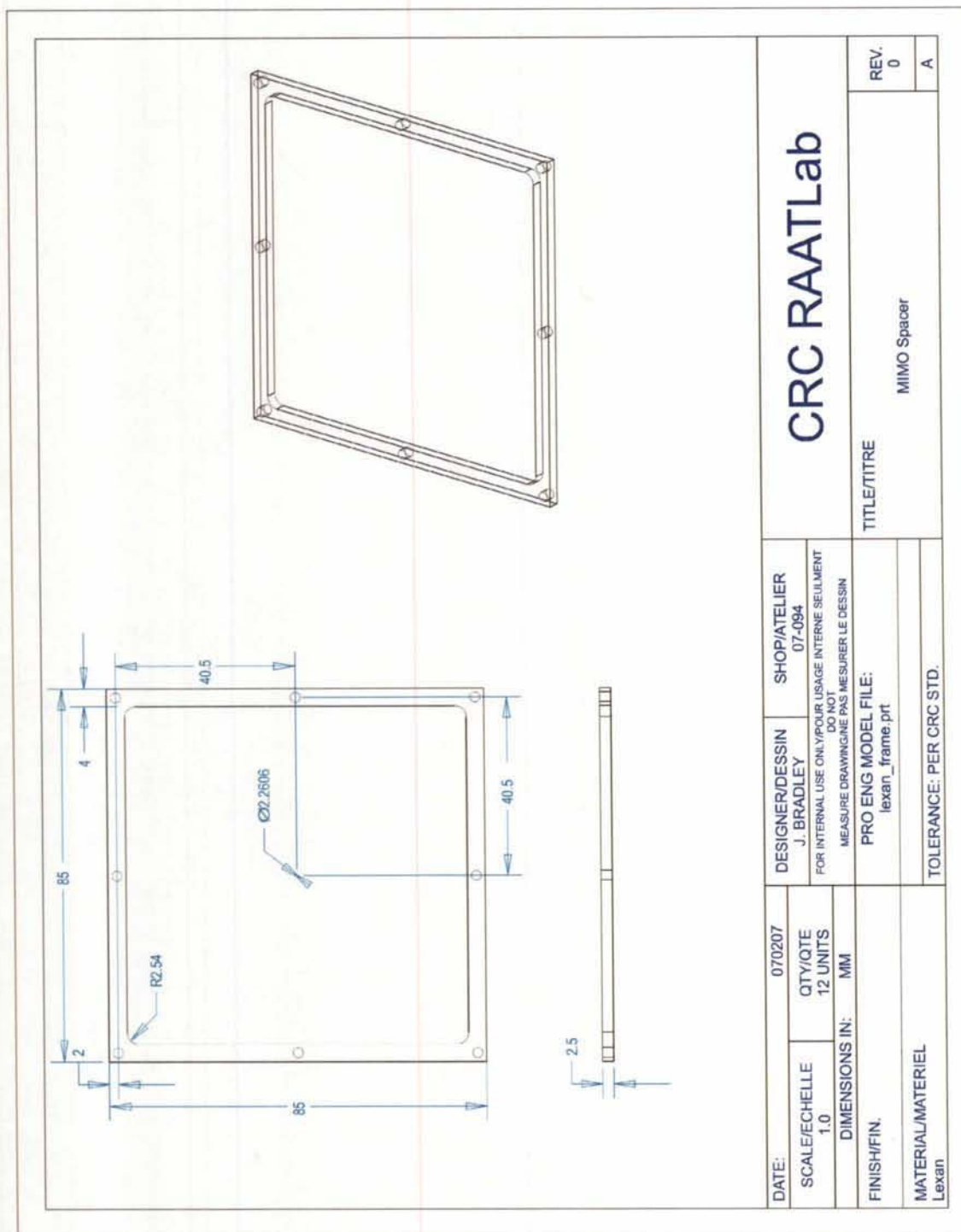


Figure 36: Lexan frame technical drawing.

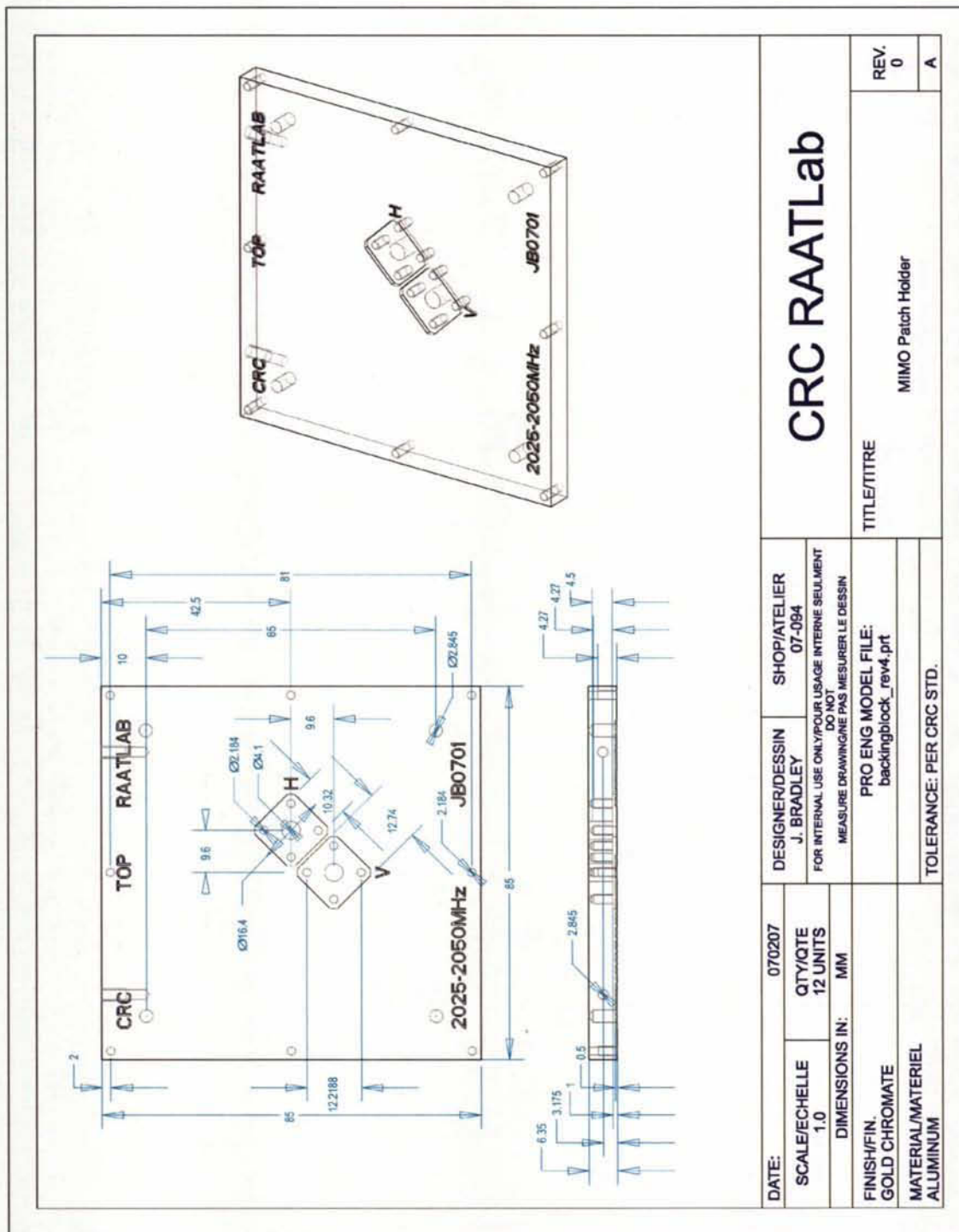


Figure 37: Thick ground plane aluminium plate technical drawing.

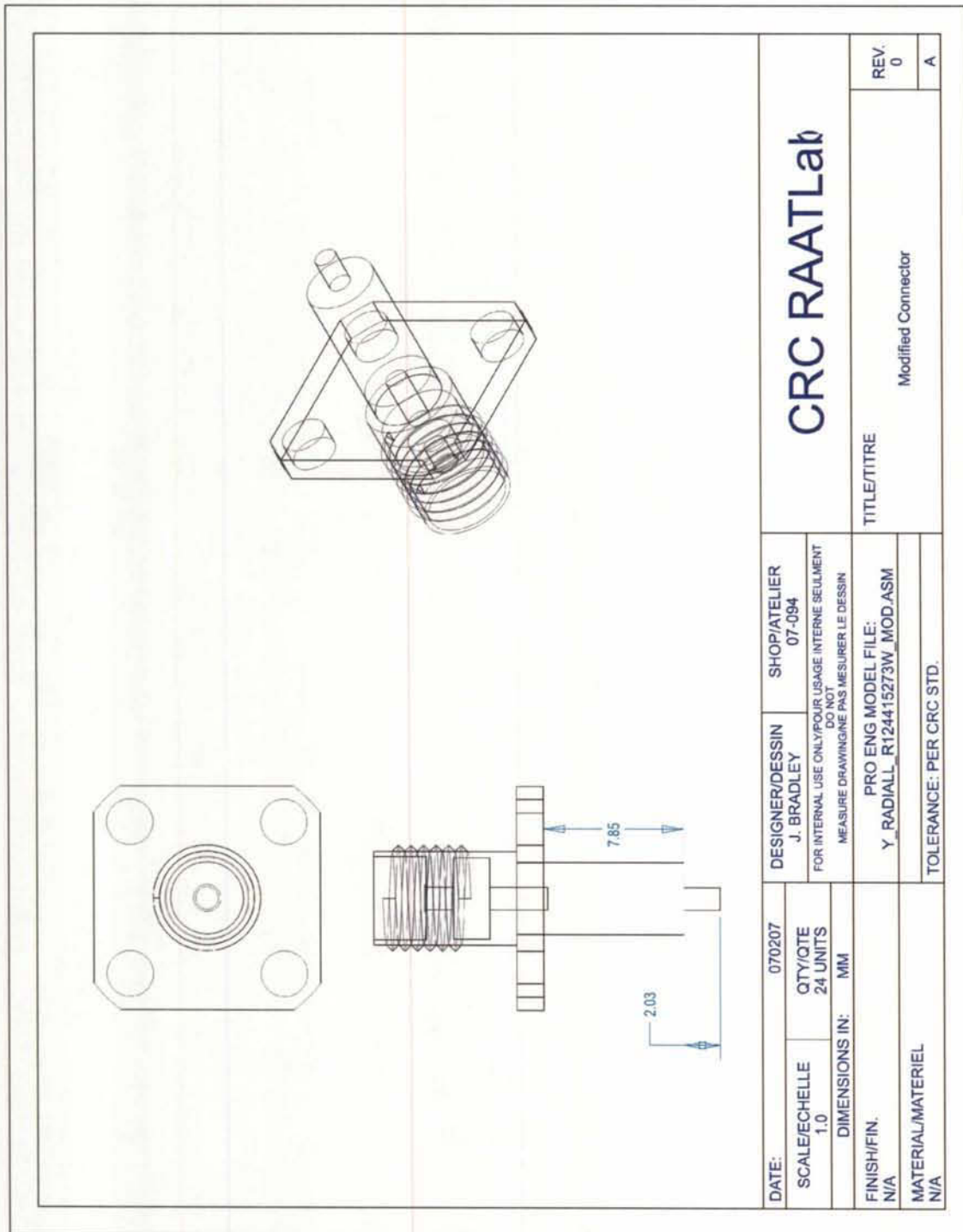
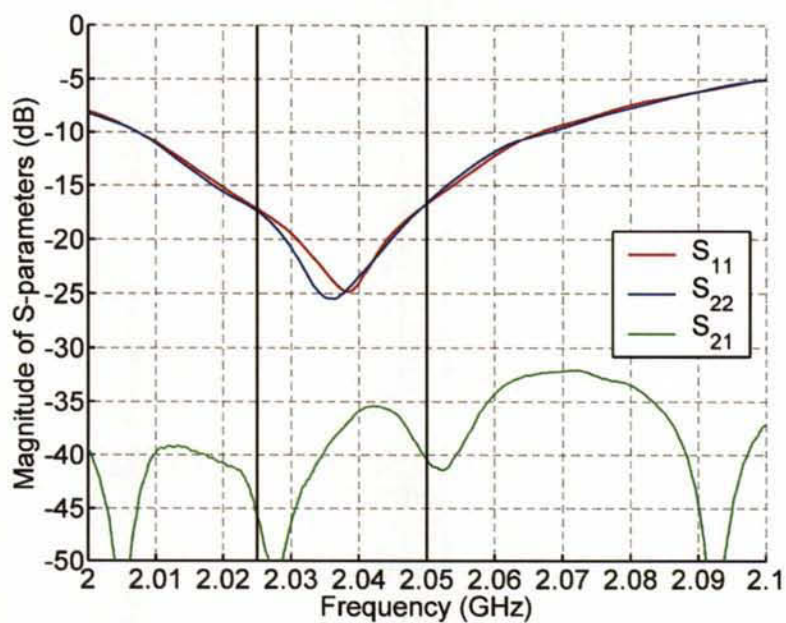
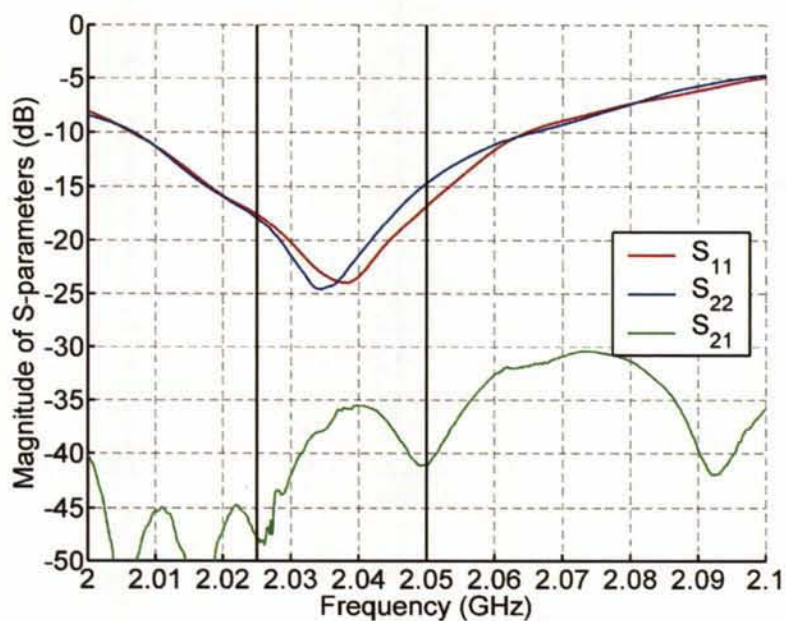


Figure 38: Connector technical drawing.

Appendix B: S-Parameter Measurement Results

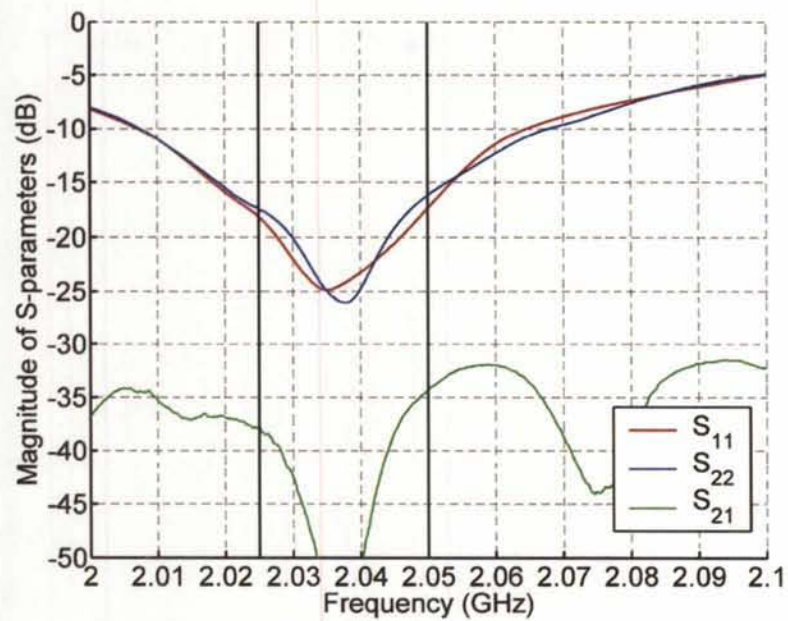


a. MIMO antenna #1

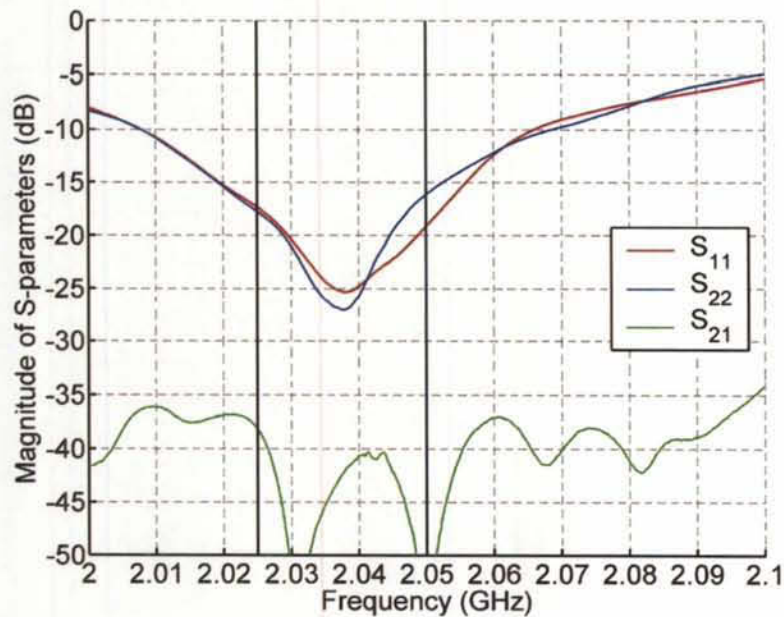


b. MIMO antenna #2

Figure 39: S-parameters measured results for MIMO antennas.

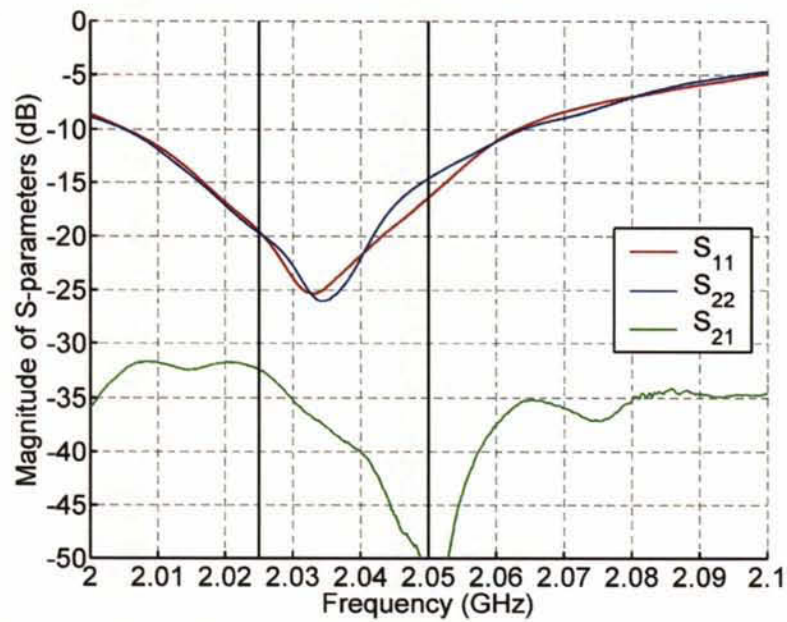


c. MIMO antenna #3

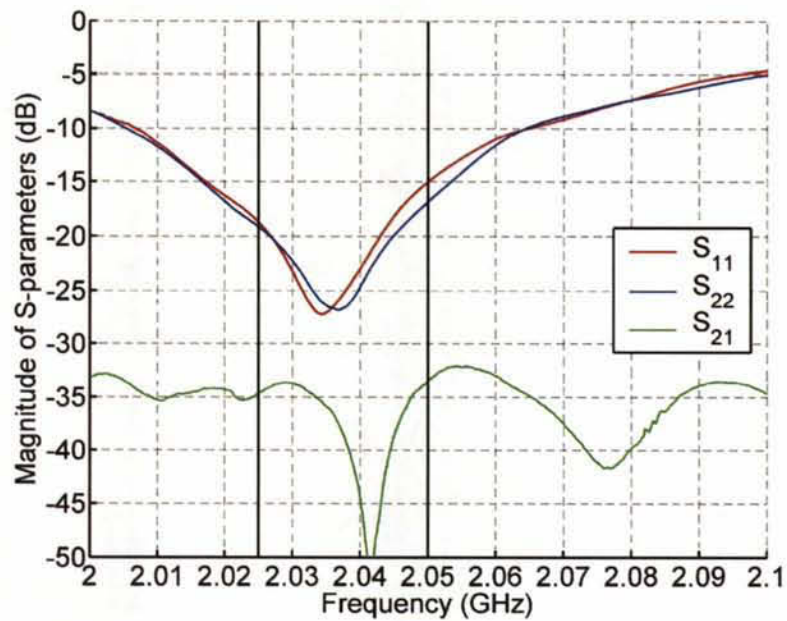


d. MIMO antenna #4

Figure 39 (continued)

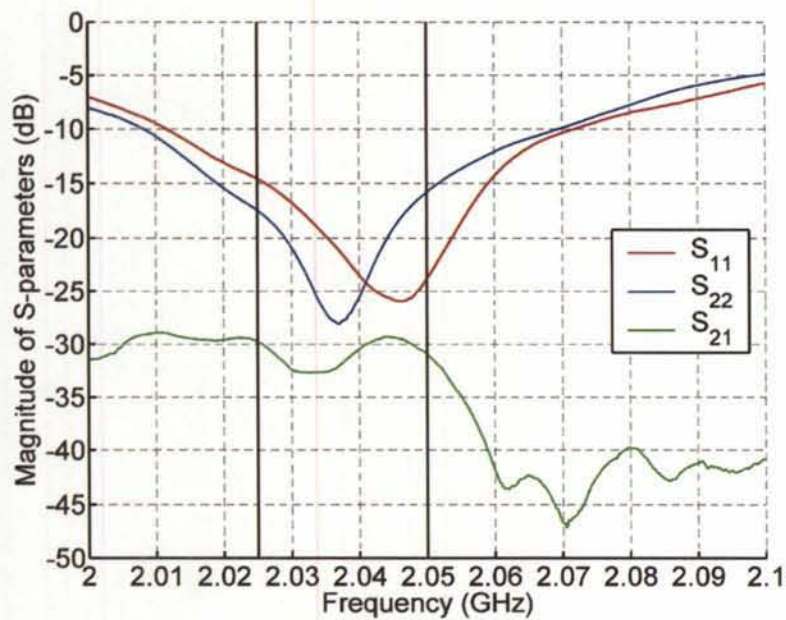


e. MIMO antenna #5

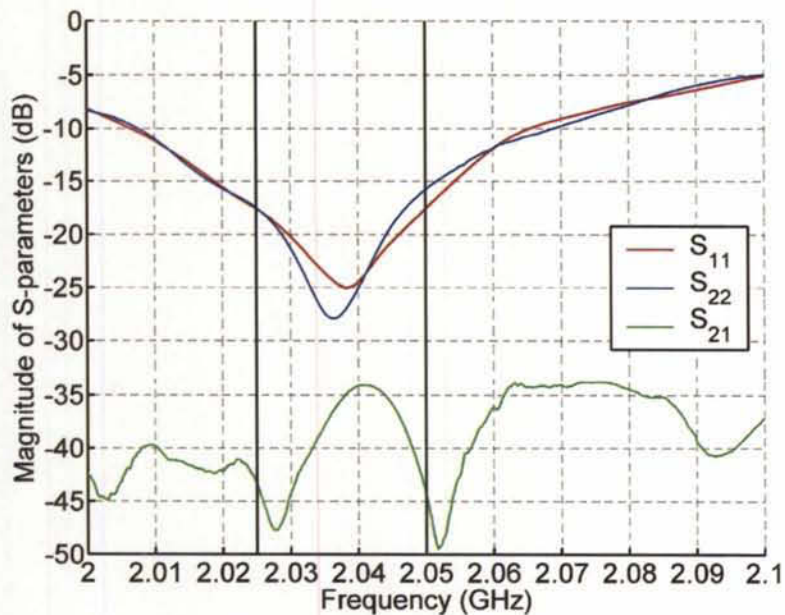


f. MIMO antenna #6

Figure 39 (continued)

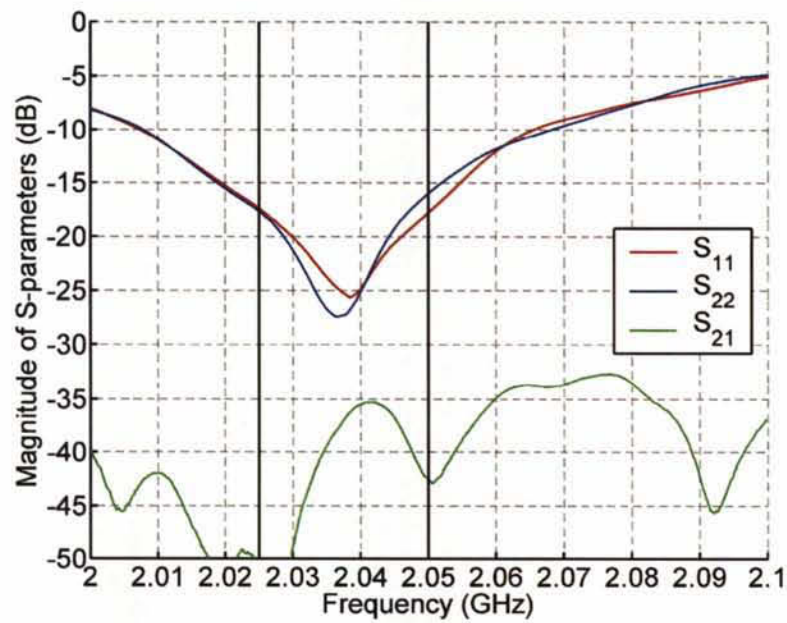


g. MIMO antenna #7

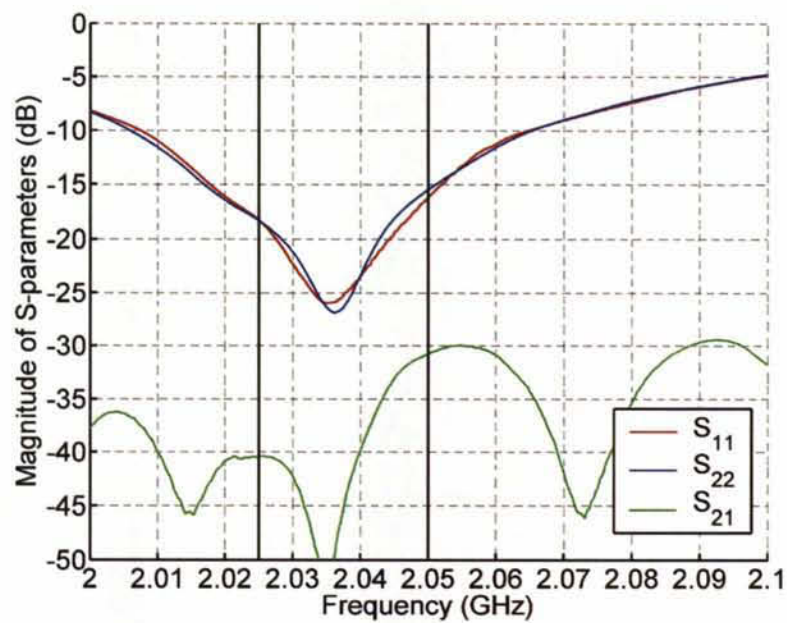


h. MIMO antenna #8

Figure 39 (continued)



i. MIMO antenna #9

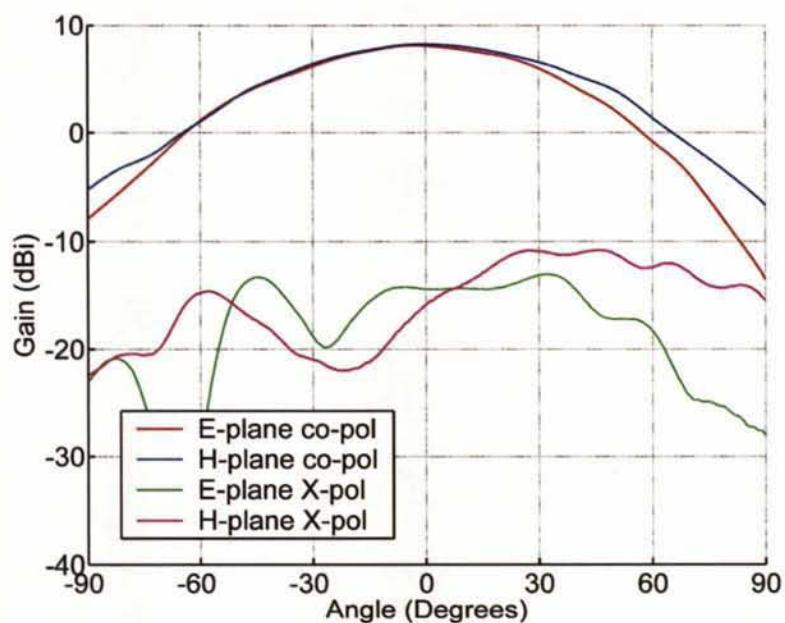


j. MIMO antenna #10

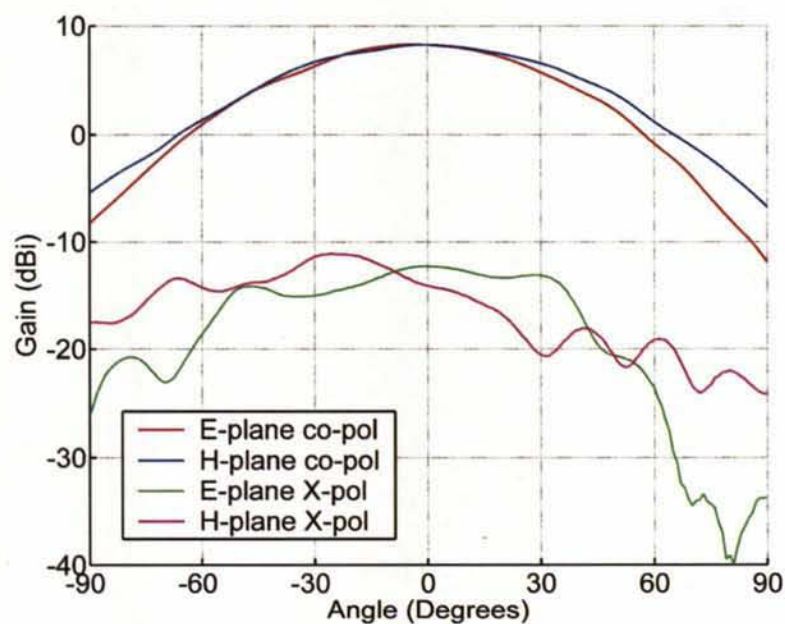
Figure 39 (continued)

<This page intentionally left blank>

Appendix C: Far-field Measurement Results

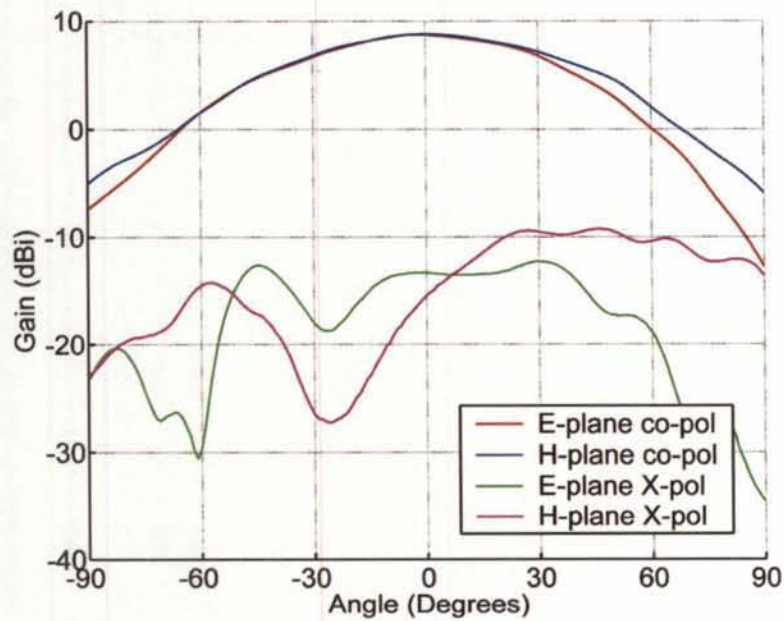


a. Port 1 (V) @ lower band (2.025 GHz)

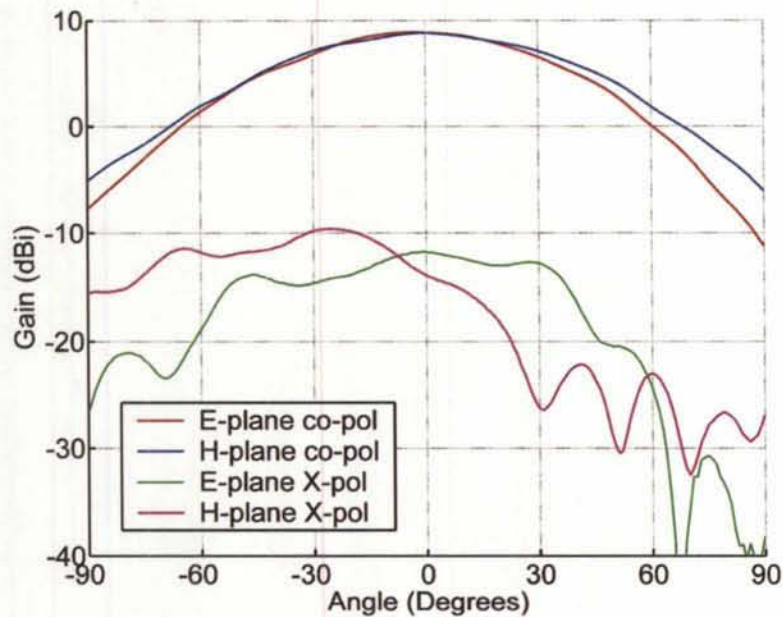


b. Port 2 (H) @ lower band (2.025 GHz)

Figure 40: Measured far-field patterns for MIMO antenna (RAATLab unit).

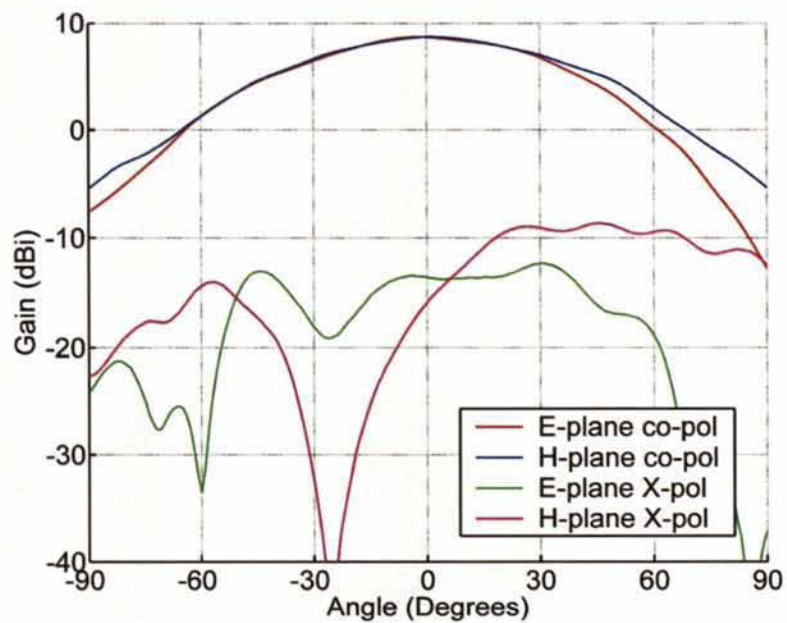


c. Port 1 (V) @ mid band (2.0375 GHz)

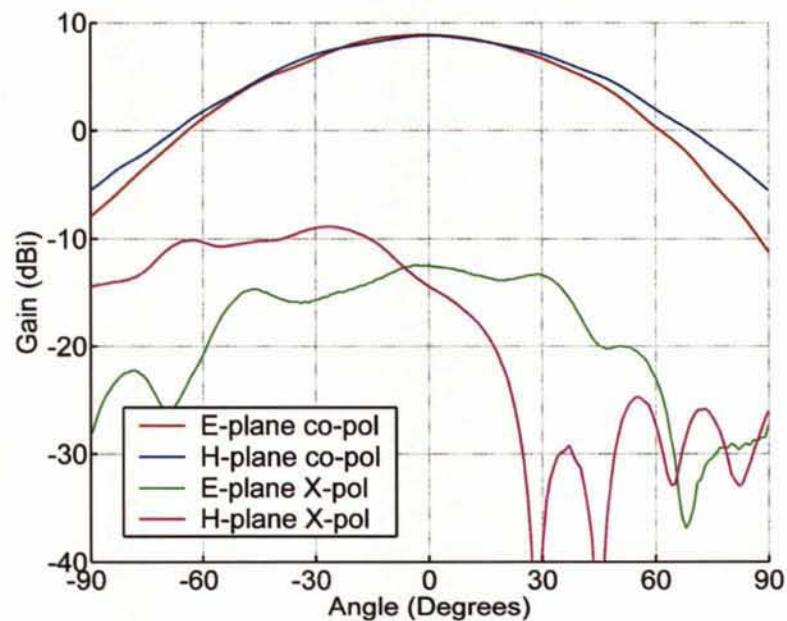


d. Port 2 (H) @ mid band (2.0375 GHz)

Figure 40 (continued)



e. Port 1 (V) @ upper band (2.050 GHz)



f. Port 2 (H) @ upper band (2.050 GHz)

Figure 40 (continued)

LKC
TK5102.5 .C673e #2007-002
Design of dual-polarized
probe-fed microstrip patch
antennas for MIMO
application

[illegible]

